nanomaterials

MDPI

Article

Methane Catalytic Combustion under Lean Conditions over Pristine and Ir-Loaded $La_{1-x}Sr_xMnO_3$ Perovskites: Efficiency, Hysteresis, and Time-on-Stream and Thermal Aging Stabilities

Catherine Drosou [1,*], Ersi Nikolaraki [1], Theodora Georgakopoulou [1], Sotiris Fanourgiakis [1], Vassilios T. Zaspalis [2,3] and Ioannis V. Yentekakis [1,4,*]

[1] Laboratory of Physical Chemistry and Chemical Processes, School of Chemical and Environmental Engineering, Technical University of Crete, 731 00 Chania, Crete, Greece; enikolaraki@tuc.gr (E.N.); theodorageorgakopoulou@gmail.com (T.G.); sfanourgiakis@tuc.gr (S.F.)
[2] Department of Chemical Engineering, Aristotle University of Thessaloniki, 541 24 Thessaloniki, Greece; zaspalis@auth.gr
[3] Chemical Process and Energy Resources Institute, Center for Research and Technology Hellas (CPERI/CERTH), 570 01 Thermi, Thessaloniki, Greece
[4] Institute of GeoEnergy, Foundation for Research and Technology-Hellas (FORTH/IG), 731 00 Chania, Greece
* Correspondence: edrosou@tuc.gr (C.D.); igentekakis@tuc.gr (I.V.Y.)

Abstract: The increasing use of natural gas as an efficient, reliable, affordable, and cleaner energy source, compared with other fossil fuels, has brought the catalytic CH_4 complete oxidation reaction into the spotlight as a simple and economic way to control the amount of unconverted methane escaping into the atmosphere. CH_4 emissions are a major contributor to the 'greenhouse effect', and therefore, they need to be effectively reduced. Catalytic CH_4 oxidation is a promising method that can be used for this purpose. Detailed studies of the activity, oxidative thermal aging, and the time-on-stream (TOS) stability of pristine $La_{1-x}Sr_xMnO_3$ perovskites (LS_XM; X = % substitution of La with Sr = 0, 30, 50 and 70%) and iridium-loaded $Ir/La_{1-x}Sr_xMnO_3$ (Ir/LS_XM) perovskite catalysts were conducted in a temperature range of 400–970 °C to achieve complete methane oxidation under excess oxygen (lean) conditions. The effect of X on the properties of the perovskites, and thus, their catalytic performance during heating/cooling cycles, was studied using samples that were subjected to various pretreatment conditions in order to gain an in-depth understanding of the structure–activity/stability correlations. Large (up to ca. 300 °C in terms of T_{50}) inverted volcano-type differences in catalytic activity were found as a function of X, with the most active catalysts being those where X = 0%, and the least active were those where X = 50%. Inverse hysteresis phenomena (steady-state rate multiplicities) were revealed in heating/cooling cycles under reaction conditions, the occurrence of which was found to depend strongly on the employed catalyst pre-treatment (pre-reduction or pre-oxidation), while their shape and the loop amplitude were found to depend on X and the presence of Ir. All findings were consistently interpreted, which involved a two-term mechanistic model that utilized the synergy of Eley–Rideal and Mars–van Krevelen kinetics.

Keywords: catalytic methane oxidation; LSM perovskites; iridium; thermal aging stability; lean conditions; hysteresis phenomena

Citation: Drosou, C.; Nikolaraki, E.; Georgakopoulou, T.; Fanourgiakis, S.; Zaspalis, V.T.; Yentekakis, I.V. Methane Catalytic Combustion under Lean Conditions over Pristine and Ir-Loaded $La_{1-x}Sr_xMnO_3$ Perovskites: Efficiency, Hysteresis, and Time-on-Stream and Thermal Aging Stabilities. *Nanomaterials* **2023**, *13*, 2271. https://doi.org/10.3390/nano13152271

Academic Editors: Jian Qi and Hui Liu

Received: 12 July 2023
Revised: 2 August 2023
Accepted: 3 August 2023
Published: 7 August 2023

1. Introduction

The replacement of traditional fossil fuels with cleaner and/or sustainable energy sources is currently imperative due to the recent global energy and environmental crisis. Regarding the global transition toward so-called "low carbon footprint energy technologies" and successful sustainability, humanity has exhibited an ever-increasing dependence upon natural gas (NG); gas is widely considered to be the 'bridge fuel' during this transition period [1–4]. NG typically contains ~85–95% methane [4–6]. The high efficiency of methane as

a fuel, as well as the associated low emissions of NO_x, CO, and particulate pollutants when producing thermal energy in urban tissues and industries, or when producing mechanical energy for vehicles, make it a greener alternative compared with other fossil fuels; this is because it produces reliable and affordable energy, and it promotes the development of other "green" energy sources [4]. In addition, its use in added-value chemical production [7–9], synthesis gas and/or H_2 production (with the simultaneous recycling of CO_2 emissions via dry reforming processes [10–15]), as well as its direct (internal) electrochemical conversion which produces electricity using solid oxide fuel cells (SOFCs) [16–20], are some additional important applications of CH_4 in cleaner energy production technologies. However, as the use of methane in this plethora of applications expands, so do the emissions of unconverted methane, most of which have a low methane content of 0.1–1.0% [21–28]. Such emissions must be urgently and effectively mitigated given that CH_4 is one of the main greenhouse gases; it has a greenhouse efficiency that is 25 times greater than CO_2, otherwise, the climate benefits of its use could be offset [1–3].

As CH_4 contains a very strong C–H bond (450 kJ/mol), its thermal combustion with air requires very high temperatures (ca. 1500 °C) compared with other HCs. Moreover, it simultaneously produces higher amounts of NO_x as by-products of the oxidation of N_2 (found in the air) in the burners operating at such high temperatures [4,5]. Therefore, the catalytic oxidation of methane is considered advantageous for controlling its end-of-pipe emissions due to the relatively low operating temperatures required; this is associated with minimal NO_x emissions. However, it is still true that the strong C–H bond in the methane molecule makes its catalytic activation, and thus its oxidation, relatively more difficult compared with other hydrocarbons. In recent years, various families of materials have been proposed as catalysts for the deep (complete) oxidation of methane, emphasizing on the activity and thermal stability of the materials, as well as their dependence on the chemical composition of the materials and the preparation method used [4,5,21–28].

In this regard, catalysts based on noble metal (NM) nanoparticles that are dispersed on oxide or mixed oxide supports are typically more active than other families of materials, but they have the disadvantages of being priced at a high cost, and they tend to gradual deactivate during operation due to the aggregation of the noble metal nanoparticles [22,27,28]. Among NMs, iridium has shown quite an encouraging performance in emission control catalysis, which involves the oxidation of CO and volatile organic compounds (VOCs), de-NO_x, and de-N_2O reactions [29–34], as well as in CH_4 reforming reactions [14,15,35,36], but their application in real systems is limited due to the high aggregation propensity of Ir nanoparticles under oxidizing conditions at elevated temperatures [37–39]. However, we have recently demonstrated that sensitive to agglomeration metal nanoparticles can be effectively stabilized through metal-support interactions induced by supports possessing a high oxygen storage capacity (OSC) and high oxygen ions mobility (labile lattice oxygen) [39–41]. A model that could consistently interpret these findings was developed. It was based on the effect of thermally driven O^{2-} ions moving from the supports onto catalyst NPs in order to create an $O^{\delta-}$ layer on their surfaces. Then, as a protective coat, it resists the main particle agglomeration mechanisms, namely, the Particle Migration and Coalescence (PMC) and Ostwald Ripening (OR) mechanisms [40,41].

On the other hand, mixed metal oxides, especially those of the perovskite class (ABO_3), combine high thermal and chemical stabilities with the adequate activity of oxidation reactions, while keeping their cost relatively low [42–46]. Perovskites based on the combination of La and Mn in the A and B sites, respectively, are among the most popular materials in the family. The partial substitution of La^{3+} by Sr^{2+} in the perovskite structure (i.e., $La_{1-x}Sr_xMnO_3$) can enhance the redox properties of the material by increasing the oxygen vacancies and the oxidation state of the B cation (Mn), introducing significant changes to their catalytic performance and their thermal stability [42–49]. Especially after the inspiring discovery of Nishihata et al. [50] and Tanaka et al. [51], who demonstrated the self-regenerative function of noble metal substituted perovskites, a phenomenon that was later called "redox exclusion" [52,53], as well as methods that determine the

nanostructure of the perovskite itself, thus improving the surface area and other catalysis-related properties [54,55], new horizons were opened for the use of perovskites in various environmental- [54,56–59] and energy- [55,60–64] related catalytic processes, which resulted in great success.

However, the classical partial substitution of the A and/or B sites of an ABO_3 perovskite with other cations, with the same or different valences, to obtain substituted (as called) $A_{1-y}A'yB_{1-x}B'_xO_{3\pm\delta}$ perovskites, remains a popular methodology for controlling the performance of perovskites due to its high flexibility. The bulk, surface, and redox properties of the original ABO_3 perovskite can be easily tailored on demand [43–47]. Emphasis is always placed on the oxygen storage capacity (OSC), oxygen ion mobility, and population of the surface oxygen vacancies (O defects) of the substituted perovskites; these properties play a key role in catalysis via oxides [56–67], as well as in catalysis via dispersed metal nanoparticles on oxide supports [13–15,68–75]. Regarding the latter, these properties are critical for the development of desirable metal–support interactions. It is therefore obvious why perovskites are a class of materials that attract high and ever-increasing interest with regard to heterogeneous catalysis; they are either used as pristine materials, exploiting their own advantageous characteristics for catalysis, or as effective supports for metal nanoparticles, as they endow them with favorable metal-support interactions.

In a previous study, the effect of the degree of the substitution of La by Sr on $La_{1-x}Sr_xMnO_3$ perovskite and their counterpart, iridium-loaded catalysts ($Ir/La_{1-x}Sr_xMnO_3$), was studied in CO oxidation with excess O_2 reaction [30]. Both catalyst series were found to be effective in the reaction, with the $Ir/La_{1-x}Sr_xMnO_3$ catalysts significantly outperforming their pristine $La_{1-x}Sr_xMnO_3$ counterparts. Interesting inverse hysteresis phenomena were observed during heating/cooling cycles, depending on both the degree of substitutional Sr (x), and the pretreatment (pre-oxidation/pre-reduction) of the catalysts. The results were part of a project to decipher the effectiveness of perovskite-based catalysts, in combination with the relatively cheap noble metal, Ir, in reactions related to the control of NG-powered vehicle emissions. Traffic caused by NG-fueled vehicles is increasing rapidly (ca. 23 million worldwide, ranging from heavy-duty to light-duty cars, with an annual increase of 20%) [4]. Catalysis of CH_4 combustion is also of particular interest because unburnt CH_4 also exists in the exhaust stream of NG-powered engines and processes [21–28,64–68]. Complete methane combustion is also a useful side process in the very demanding application of natural-gas (NG) fueled gas-turbines (GT), as they operate alongside the catalytically stabilized hybrid combustion concept [76].

In the present work, lean CH_4 combustion on pristine $La_{1-x}Sr_xMnO_3$ (LS_XM; X = 0, 30, 50 and 70% substitution of La with Sr) perovskites and their 2 wt% iridium loaded counterparts (Ir/LS_XM) is comparatively studied in a temperature range of 400–970 °C. The impact of the degree of substitution of the A-site (La) of the perovskite with Sr, on its catalytic behavior is explored. This occurs after an exploration into the catalysts' various pre-treatment protocols, such as pre-reduction, pre-oxidation, and thermal aging, which were implemented to obtain a complete overview of their CH_4 combustion performance and how it correlates with the morphological characteristics and properties of the materials. Complex hysteresis phenomena recorded for the first time using this catalyst/reaction system during heating/cooling cycles were therefore consistently interpreted. Although LSM perovskites are possibly among the most studied materials for their catalytic performance in various reactions, not excluding some studies concerning the oxidation of CH_4, the highly systematic activity and stability studies performed herein revealed new phenomena and findings that could be both of specific and general interest for catalysis research.

2. Materials and Methods

2.1. LSxM and Ir/LSxM Catalysts Synthesis

The unloaded and 2 wt% Ir loaded perovskite-type $La_{1-x}Sr_xMnO_3$ (denoted hereafter as LSxM, where x = 0, 30, 50 and 70 expresses the % replacement of La with Sr in the perovskite formula) catalysts were prepared using the co-precipitation method described

by Haron et al. [77]. The nitrate salts, $La(NO_3)_3 \cdot 6H_2O$ (VWR Chemicals, 99.9%), $Sr(NO_3)_2$ (Sigma Aldrich, St. Louis, MO, USA, 99.0%) and $Mn(NO_3)_2 \cdot 6H_2O$ (Panreac, Darmstadt, Germany, 98.0%), were used as metal precursors. In brief, appropriate amounts of the nitrate salts were diluted in distilled water and added to a NaOH (VWR Chemicals, Radnor, PA, USA, 98.9%) precipitating agent solution for co-precipitation. The obtained suspension was filtered, washed, dried, de-agglomerated, and finally calcined in air at 1000 °C for 6 h for the final perovskite structure to be obtained. A series of $LS_{00}M$, $LS_{30}M$, $LS_{50}M$ and $LS_{70}M$ perovskites were produced.

Half of each perovskite was then impregnated under continuous stirring conditions at 75 °C in an appropriate amount of aqueous solution comprising $IrCl_3 \cdot H_2O$ (Abcr GmbH & Co KG) with 2 mg Ir/mL in order to achieve the corresponding 2 wt% Ir/LS_XM catalyst series. After the water evaporated, the obtained suspensions were dried at 110 °C for 12 h; then, they were subjected to reduction at 400 °C for 3 h in a 50 mL/min flow of 25% H_2/He to remove residual chlorine and to avoid the formation of large Ir crystallites [32,33]. The as-prepared LS_XM and Ir/LS_XM catalyst series are listed in Table 1.

Table 1. The LS_XM (X = % substitution of La with Sr) and 2wt% Ir/LS_XM series of catalysts studied. A summary of their chemical formulas, textural, morphological, and oxygen storage capacity characteristics [30].

Catalysts Code	Chemical Formula	S_{BET} (m^2/g)	Average Pore Diameter (nm)	Total OSC (μmol O_2/g)	Mean Ir Particle Size (nm)
$LS_{00}M$	$LaMnO_3$	12.0	10.9	671	n.a
$LS_{30}M$	$La_{0.7}Sr_{0.3}MnO_3$	10.4	9.8	766	n.a
$LS_{50}M$	$La_{0.5}Sr_{0.5}MnO_3$	6.8	8.9	886	n.a
$LS_{70}M$	$La_{0.3}Sr_{0.7}MnO_3$	11.3	8.8	1219	n.a
$Ir/LS_{00}M$	2 wt% $Ir/LaMnO_3$	9.7	11.9	753	1.1
$Ir/LS_{30}M$	2 wt% $Ir/La_{0.7}Sr_{0.3}MnO_3$	10.5	10.0	981	1.1
$Ir/LS_{50}M$	2 wt% $Ir/La_{0.5}Sr_{0.5}MnO_3$	6.2	8.1	1203	1.0
$Ir/LS_{70}M$	2 wt% $Ir/La_{0.3}Sr_{0.7}MnO_3$	11.0	13.7	1348	1.2

2.2. Catalyst Characterization Methods

The textural and structural characteristics and redox properties of the LS_XM and Ir/LS_XM catalysts were determined using the N_2 physical adsorption BET–BJH method, powder X-ray diffraction (XRD), isothermal pulse H_2-chemisorption (H_2-Chem.), and Temperature programmed reduction using hydrogen (H_2-TPR).

More specifically, the Brunauer–Emmett-Teller (BET) method and Barrett–Joyner–Halenda (BJH) model were used to analyze N_2 adsorption–desorption isotherms obtained at −196 °C, and relative pressures in the range of 0.05–0.3, using a Quantachrome Nova 2200 e instrument. Subsequently, 150 mg of the sample placed in the instrument holder was degassed for 12 h using a vacuum at 350 °C, prior to measurements. The total specific surface area (S_{BET}), the pore volume, and the average pore size diameter of the materials were obtained.

The powder X-ray diffraction (PXRD) patterns of pre-oxidized samples (calcinated in the air at 400 °C for 1 h before the XRD measurements) were collected with a BrukerAXS D8 Advance diffractometer operating at 35 kV and 35 mA, using Cu Kα radiation and a LynxEye detector with a Ni-filter, to determine the crystalline structure of the materials. Measurements were carried out in a 2θ angle range of 4–70 degrees, with a scanning speed of 0.5 degrees per min. The identification and quantification of the phases were performed using BrukerAXS Topas software (COD, Crystallography Open Database) and the Rietveld method.

Pulse hydrogen chemisorption (H_2-chemisorption) experiments were performed at 25 °C on a Quantachrome/ChemBet Pulsar TPR/TPD instrument equipped with an Omnistar/Pfeiffer Vacuum mass spectrometer to determine iridium dispersion and mean iridium particle size. An amount of 150 mg of the material was loaded on the instrument

holder, which was pretreated with a 5% H_2/He mixture (15 mL/min) at 550 °C for 1 h. Then, it was flushed with N_2 (15 mL/min) at the same temperature for 30 min, and cooled to 25 °C using a N_2 flow, before consecutive pulse injections of pure hydrogen (280 μL H_2 per pulse) were imposed until saturation was reached. This was carried out in order to measure the total H_2-uptake (V_{chem}). The V_{chem} values were then used to calculate iridium dispersion, D_{Ir} (dimensionless, H/Ir ratio), and mean Ir crystallite size, d_{Ir} (in nm) via the following set of Equations (1) and (2) [15,30]:

$$D_{Ir}(H/Ir) = \frac{V_{Chem} \cdot F_s \cdot A_{Ir}}{V_{mol} \cdot X_{Ir}} \quad (1)$$

$$d_{Ir}(nm) = \frac{6 \cdot A_{Ir} \cdot 10^{20}}{D_{Ir} \cdot \rho_{Ir} \cdot \alpha_{Ir} \cdot N_{AV}} \quad (2)$$

where, V_{Chem} (mL/g) is the H_2-uptake in the chemisorption experiment, F_s is the hydrogen to metal correlation factor (=2 assuming the one-to-one correlation of adsorbed H atoms with metal sites (i.e., H–Ir)), A_{Ir} is the atomic weight of iridium (192.22 g/mol), V_{mol} is the molar volume of an ideal gas at room temperature and 1 atm pressure (ca. 24,450 mL/mol), X_{Ir} is the iridium content of the catalyst (g_{Ir}/g_{cat}), ρ_{Ir} is the Ir metal density (22.5 g/mL), α_{Ir} is the cross-sectioned area of the Ir atom (0.12 nm^2/atom), $N_{AV} = 6.023 \times 10^{23}$ molecules/mol is the Avogadro number, and 10^{20} is a unit conversion factor when the units of the parameters in Equations (1) and (2) are used as indicated above.

Temperature-programmed reduction (H_2-TPR) was performed using the same instrumentation for H_2-chemisorption experiments in order to obtain the reducibility characteristics and determine the total oxygen storage capacity (t-OSC) of the materials. The samples (150 mg) were oxidized in situ at 750 °C for 30 min (20% O_2/He flow), then, they were cooled to 25 °C using the same flow, purged for 10 min with He flow. Next, the TPR experiment was performed with a linear (10 °C/min) increase in temperature, up to 750 °C, using 15 mL/min of 1% H_2/He flow. The time integral of the H_2-TPR profile determines the total oxygen storage capacity (t-OSC) of the material [13,15,30].

2.3. Catalytic Activity and Stability Evaluation Experiments

The catalytic activity and thermal stability experiments were performed in a continuous flow experimental apparatus (Figure S1) consisting of the following: (i) a feed unit utilizing MKS-247 mass flow meters, (ii) a reactor unit with a tubular fixed-bed type reactor (quartz, ID = 3 mm), and (iii) an analysis unit equipped with online gas chromatography (SHIMADZU GC-14B, a thermal conductivity detector, He carrier gas, Porapak-N, and Molecular Sieve 5A columns connected in parallel). The reactor was loaded with m_{cat} = 50 mg of a catalyst in the form of a powder (particle size 180–250 μm). A K-thermocouple, centered in the catalyst bed, was used to measure the reaction temperature. The volume of the catalytic bed was ca. 0.03 cm^3.

Catalysts were comparatively evaluated for the CH_4 combustion reaction under conditions of excess O_2 (1% CH_4 + 5% O_2, balance He at 1 bar) at a weight-basis Gas Hourly Space Velocity (WGHSV) equal to 90,000 mL/g·h (total flowrate F_T = 75 mL/min), in the temperature range of 400–970 °C; this corresponds with the operating temperature window of vehicle emission control systems (in particular, of close-coupled catalytic converters). The residence time of the reactants is ca. τ = 0.023 s (i.e., a gas hourly space velocity, GHSV, of ca. 156,500 h^{-1}). The 'light-off' behavior of the catalysts (CH_4 conversion versus temperature in constant reactor feed conditions) was obtained by increasing the temperature stepwise (~30 °C/step); in other words, they remained at each temperature for ~20 min to ensure a steady-state operation.

Both the pre-reduced and pre-oxidized states of the catalyst were evaluated by respectively applying the following pretreatment conditions, prior to light-off measurements: (i) pre-reduction at 600 °C for 2 h with a 50 mL/min flow of 25% H_2/He, and (ii) pre-oxidation at 400 °C for 1 h with a 50 mL/min flow of 20% O_2/He. In addition, 12 h of

time-on-stream (TOS) stability experiments were performed at a constant temperature, which was different for each catalyst, and equal to that of its corresponding T_{50} (temperature for 50% CH_4 conversion). Finally, resistance against the deactivation of the LS_XM and Ir/LS_XM counterpart catalysts, after the imposition of stressed oxidative thermal aging conditions, was studied by imposing 5 h in situ oxidation at 750 °C with a 20% O_2/He flow; then, a re-evaluation of catalyst performances under the same reaction conditions that were previously applied took place. All the above steps, and the order in which they were performed, are shown in Scheme 1.

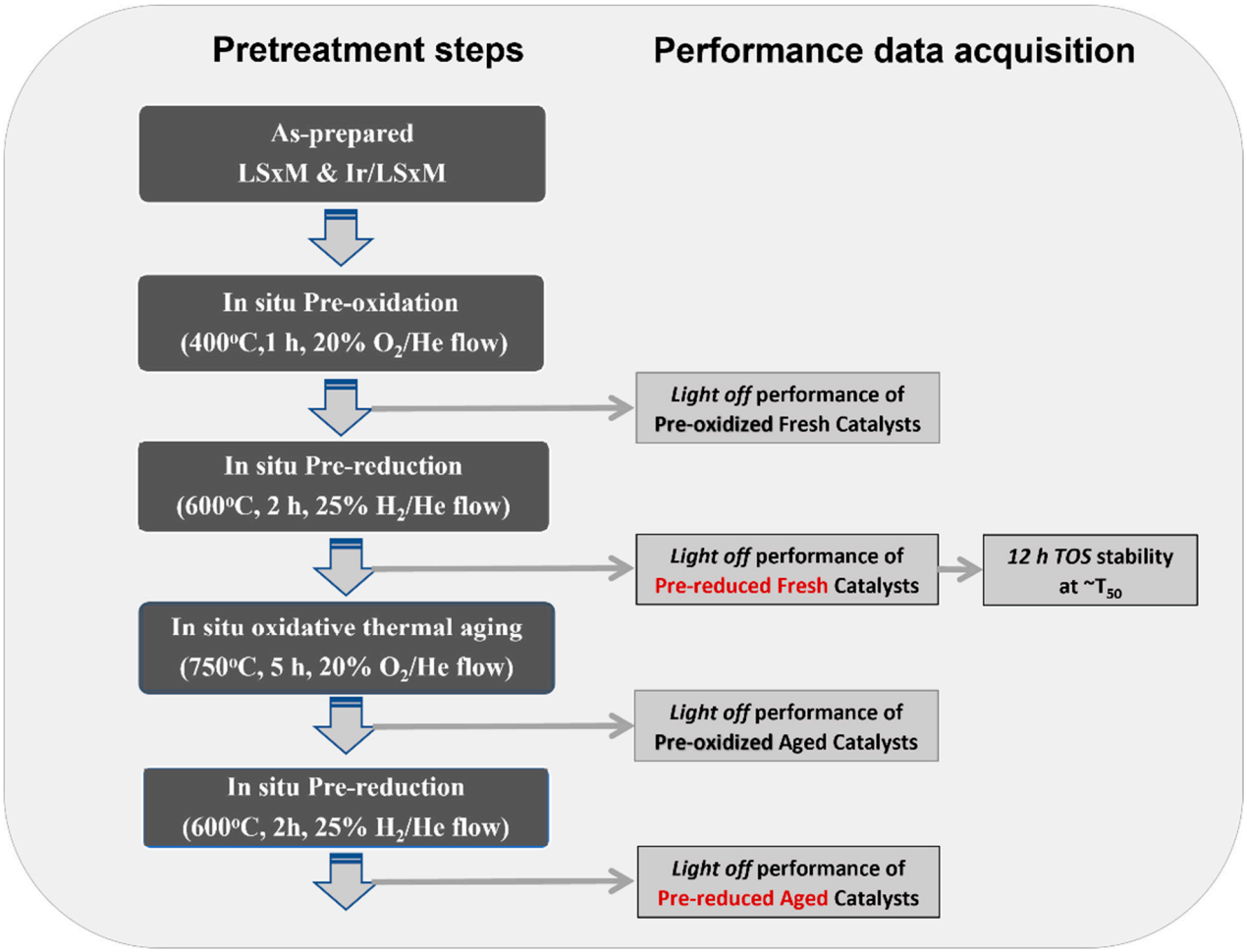

Scheme 1. Experimental procedure followed for LS_XM and Ir/LS_XM catalysts efficiency and stability evaluation under the complete oxidation of CH_4 reaction. The evaluation was always performed under reaction conditions comprising 1.0% CH_4 + 5.0% O_2 + 94% He, p = 1 bar, and WGHSV = 90,000 $cm^3/g{\cdot}h$ (F_T = 75 cm^3/min, m_{cat} = 50 mg).

The conversion of CH_4 (X_{CH4}) is calculated using Equation (3), as follows:

$$X_{CH_4}(\%) = 100\frac{F_{in}[CH_4]_{in} - F_{out}[CH_4]_{out}}{F_{in}[CH_4]_{in}} \quad (3)$$

where F is the total gas flow rate (mL/min), $[CH_4]$ is the v/v fraction of CH_4 in the gas stream, and the subscripts "in" and "out" indicate the reactor inlet and outlet gas streams, respectively.

3. Results and Discussion

3.1. Catalyst Characteristics and Physicochemical Properties

A thorough characterization of the LS_XM and Ir/LS_XM materials has been previously performed and can be found in [30]. The textural, morphological, and total oxygen storage capacity (t-OSC) characteristics are summarized in Table 1 and described in detail below.

The specific surface area (S_{BET}) values of the materials were between 6.8–12 m^2/g, which are quite low, but typical for perovskite-type materials. The substitution of La with Sr, up to when X = 50%, decreased S_{BET} monotonically from 12 to 6.8 m^2/g, which then increased again for when X = 70%, as it approached the initial value. Perovskites are considered to be ionic materials consisting of closed-packed arrays of relatively large oxygen ions. Under these conditions the rate controlling step for densification during sintering comprises the diffusion of the oxygen anions; this takes place through oxygen vacancies rather than through interstitial sites. The addition of the substituted Sr, was compensated with Mn^{4+} cations, the reduction of which, upon heating at 1000 °C, creates oxygen vacancies. These enhance the oxygen anion diffusion rate, and consequently, the densification rate. This explains the gradual S_{BET} reduction, along with the increasing Sr content. The subsequent increase in S_{BET}, at higher Sr contents, indicates that at Sr contents higher than 0.5, the defect chemistry of the system changes and is not dictated by the same rules. In addition, the presence of secondary phases, even at small amounts, is able to significantly influence densification during sintering at 1000 °C.

The addition of Ir via impregnation reduced the value of S_{BET} due to the partial blocking of the LS_XM small-sized pores, caused by the Ir nanoparticles. This is evidenced by the slightly higher average pore size values of Ir/LS_XM compared with their LS_XM counterparts (Table 1).

The average size of Ir nanoparticles was estimated to be in the order of 1.0–1.2 nm (Table 1) using Equations (1) and (2) fitted with the H_2-uptake values obtained from the isothermal H_2-chemisorption experiments. The corresponding Ir dispersion values (D_{Ir}) ranged between 61% and 73%.

The structural characteristics of the materials obtained via the analysis of their XRD patterns confirmed the development of the lanthanum manganate perovskite structure at an angle of 2θ~32.4–33.1° (Figure S2 in the Supplementary Materials file). Other secondary phases of single or mixed oxides, appearing mainly in the material with the higher substitutions of La with Sr (X = 70%), can be seen in Figure S2. The main peak of the perovskite structure, at about 33°, is magnified in Figure S3, wherein a gradual transition from a rhombohedral to a cubic structure (with increasing Sr content) is clearly distinguishable from the splitting of the peak at a diffraction angle 2θ~32–33°. In addition, there is a shift to larger angles as the substitution of La with Sr increases; this indicates that the unit cell is being contracted [47,48]. This cell contraction most likely resulted from the oxidation of Mn^{3+} to Mn^{4+} when the Sr content of the material increased, rather than from the creation of oxygen vacancies, which, if they occurred, would lead to unit cell expansion [47,48]. Moreover, the appearance of other crystalline phases of single or mixed oxides, along with the perovskite structure, appeared in materials with higher substitutions of La with Sr (x = 70%). On the other hand, no Ir species were detected in the XRD diffractograms of Ir/LS_XM catalysts, which is most likely due to its small-sized nanoparticles (~1 nm); this indicates successful dispersion.

The reducibility characteristics of the LS_XM perovskites are shown in the H_2-TPR profiles of Figure 1. The total oxygen storage capacity (t-OSC) of each perovskite, obtained from the integrated area of their respective TPR profiles in the time interval of the experiment [13,30], are given in Table 1. Values range from 670 to 1350 μmol O_2/g, increasing systematically with increasing levels of X.

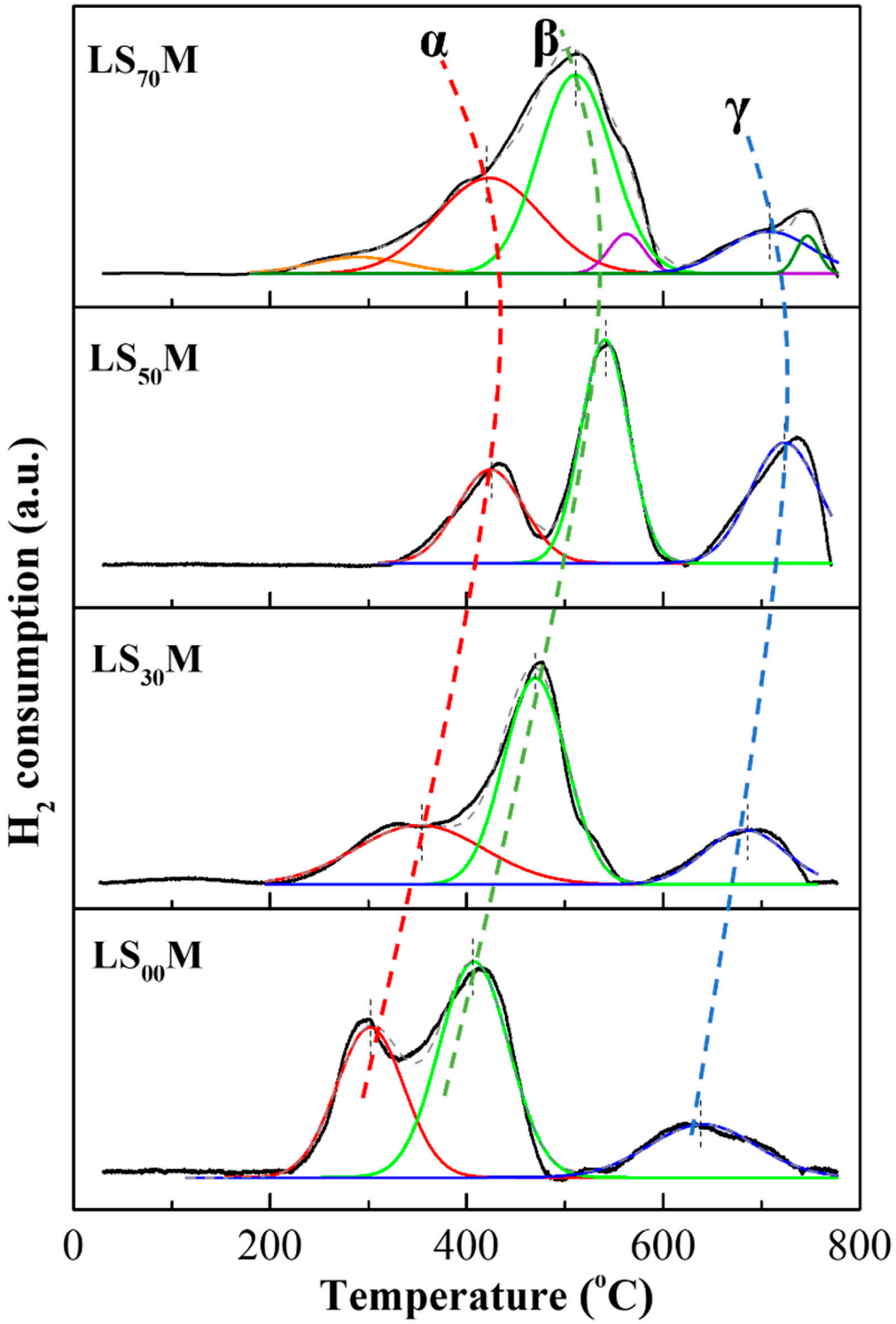

Figure 1. H_2-TPR profiles for the LS_XM catalysts and main peak deconvolutions. Peak (α) → O_{ads}; peak (β) → Mn^{4+} to Mn^{3+} reduction; peak (γ) → Mn^{3+} to Mn^{2+} reduction.

The deconvolution of the broad overlapping peaks in the TPR profiles of LS_XM reveals three main peaks (α, β, and γ) for the perovskites with compositions where X = 0–50%, whereas additional, lower intensity peaks appear when X = 70%. The three main α, β, and γ kinds of oxygen are placed at temperature regions of ca. 200–450 °C, 350–600 °C, and 600–800 °C, respectively; their reduction regions gradually shift to higher temperatures by

increasing X until X = 50%, then, they shift again to lower temperatures when X = 70%, in accordance with Ponce et al. [78].

In accordance with the literature, peak α is attributed to adsorbed surface oxygen species, O_{ads}; peak β is attributed to the labile lattice oxygen, thus reflecting the Mn^{4+}/Mn^{3+} redox couple (Equation (4)) caused by the reduction of high-valence Mn^{4+} to Mn^{3+}; and finally, peak γ is attributed to the labile lattice oxygen reflecting the Mn^{3+}/Mn^{2+} redox couple (Equation (5)) caused by the reduction of Mn^{3+} to Mn^{2+} [25,44,78–83]. Equations (2) and (3) are written in accordance with the Kröger–Vink notation, as follows [84]:

$$O_O^{\times} + 2Mn_{Mn}^{\bullet} \overset{Mn^{4+}/Mn^{3+}}{\Longleftrightarrow} 2Mn_{Mn}^{\times} + V_O^{\bullet\bullet} + \frac{1}{2}O_2(g) \quad (4)$$

$$O_O^{\times} + 2Mn_{Mn}^{\times} \overset{Mn^{3+}/Mn^{2+}}{\Longleftrightarrow} 2Mn_{Mn}^{\prime} + V_O^{\bullet\bullet} + \frac{1}{2}O_2(g) \quad (5)$$

where the reference valence for manganese is considered to be +3.

As we shall see below, LS_XM perovskites are active during lean CH_4 combustion in the entire temperature region of ca. 250–800 °C, indicating that depending on the operation temperature, all these oxygen types could potentially contribute to the overall methane consumption rate.

Considering the combined XRD and H_2-TPR findings, it may be concluded that the higher the X, the higher the M^{4+} state content in pre-oxidized LS_XM, and consequently, the higher the OSC of the material (Table 1). On the other hand, the tendency to reduce manganese (i.e., the lability of lattice oxygen, peaks β and γ) becomes progressively more difficult with increasing levels of X, up to 50%; then, for X = 70%, this is reversed (Figure 1). This can be understood if one considers that gradually increasing quantities of Mn^{4+} are needed to compensate for the Sr^{2+} additions; this finding is in accordance with the results reported in the literature [78], and it is reflected by the fact that the equilibrium constant of the reaction (4) is reported to decrease with increasing levels of X [85].

The addition of Ir to LS_XM shifts the reducibility peaks of the obtained Ir/LS_XM material to temperatures as low as ca. 150–400 °C, in which narrow temperature range encompassing all peaks (reflecting $Ir^{4+} \rightarrow Ir^0$, $Mn^{4+} \rightarrow Mn^{3+}$ and $Mn^{3+} \rightarrow Mn^{2+}$ reductions) they substantially overlap (Figure S4). This noble metal-induced enhancement of the support's reducibility is due to an increased spillover of hydrogen atoms from the noble metal particles to the reducible support, thus promoting the reducibility of the latter [74].

The additional, low-intensity peaks that appeared at temperatures of ca. 280, 560, and 750 °C on the $LS_{70}M$ H_2-TPR spectrum presumably originate from the reduction of the additional oxide phases that appear to be present in the XRD pattern of this perovskite (Figure S2). For example, manganate oxide phases can present with reduction peaks at low and intermediate temperature regions following successive reduction processes ($MnO_2 \rightarrow Mn_2O_3 \rightarrow Mn_3O_4 \rightarrow MnO$) [86]. However, the low amount of these phases detected on $LS_{70}M$ only marginally affects the overall qualitative/quantitative reducibility behavior of the material, which is still mainly determined by the α, β, and γ peaks (Figure 1).

3.2. Light-Off/Light-Out Performance of LS_XM and Ir/LS_XM Catalysts

Following the experimental schedule described in Scheme 1 for catalytic performance data acquisition, the light-off (heating)/light-out (cooling) temperature cycles were conducted after different pre-treatment stages, involving fresh or aged (at 750 °C), pre-oxidized or pre-reduced, LS_XM and Ir/LS_XM catalysts, respectively. The results of the catalytic behavior, in the order they were obtained (Scheme 1), are discussed below (i.e., first those concerning fresh catalysts are discussed, followed by those concerning thermally aged catalysts, and so on).

3.2.1. Pre-Oxidized Fresh LS_XM and Ir/LS_XM Catalysts

Figure 2 shows the performance of fresh pre-oxidized LS_XM (Figure 2a) and Ir/LS_XM (Figure 2b) catalysts during a heating/cooling cycle. The corresponding T_{50} values (temperature for 50% conversion of CH_4) are presented in Figure 2c.

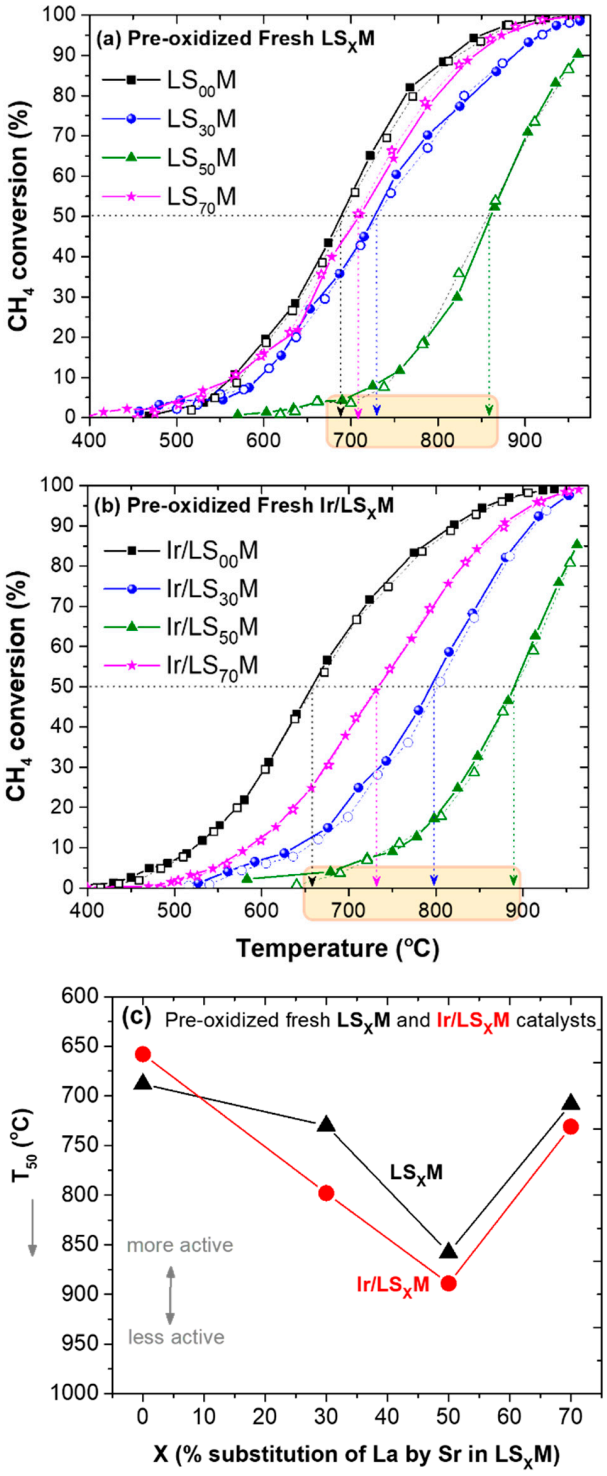

Figure 2. Light-off/light-out behavior of pre-oxidized fresh LS_XM (**a**) and Ir/LS_XM (**b**) catalysts, and the corresponding T_{50} values as a function of X (**c**). Feed conditions: 1.0% CH_4 + 5.0% O_2, He balance at 1 atm, F_T = 75 mL/min, m_{cat} = 50 mg, WGHSV = 90,000 mL/g·h. Solid symbols and lines in (**a**,**b**) show the heating path, and the open symbols and dashed lines show the cooling path of the cycle.

It is apparent that the light-off (heating) and light-out (cooling) performances of the CH_4 conversion coincide to a reasonable extent. Therefore, no hysteresis phenomena were observed. However, the activity of the catalysts appears to be strongly dependent on the La substitution with Sr (X) in the perovskite, which can be seen more clearly with the variation in T_{50} versus X (Figure 2c). This dependence, which is qualitatively similar for the two series of materials (LS_XM and Ir/LS_XM), is not monotonic, showing inverted volcanic behavior (with respect to activity), with the $LS_{50}M$ and $Ir/LS_{50}M$ pair appearing to be the less active. Furthermore, and rather unexpectedly, the iridium-loaded perovskites (Ir/LS_XM) appear typically less active than their pristine perovskite counterparts (LS_XM).

3.2.2. Pre-Reduced Fresh LS_XM and Ir/LS_XM Catalysts

The light-off (heating)/light-out (cooling) behaviors for the two sets of fresh catalysts, LS_XM and Ir/LS_XM, starting from their pre-reduced state, are depicted in Figure 3. After this pretreatment, the behavior of the catalysts appears more complex than their pre-oxidized counterparts, as it involved hysteresis phenomena (steady-state rate multiplicity) [30,87–90]. Both kinds of hysteresis were obtained for the pre-reduced samples during heating/cooling cycles (i.e., normal (counterclockwise) or inverse (clockwise) hysteresis as commonly described in the literature [87], although the latter is clearer (more intense)). In particular, the pair ($LS_{00}M$, $Ir/LS_{00}M$), when X = 0%, follows normal hysteresis (with the activity possessing higher values upon cooling), whereas those with intermediate values, regarding the Sr substitution (X = 30 and 50%), obey inverse hysteresis. The hysteresis behavior of the pair ($LS_{70}M$, $Ir/LS_{70}M$), with the maximum (X = 70%) substitution of La with Sr, is complicated; the former catalyst follows normal hysteresis, and the latter follows inverse hysteresis, although, the amplitude of the hysteresis loop in both cases is limited. Interestingly, the hysteresis loops between the counterpart catalysts, LS_XM and Ir/LS_XM, are mirrored with respect to their qualitative characteristics, suggesting that hysteresis mainly originates from the perovskite compartment of the catalyst, rather than from Ir. The latter mainly affects the hysteresis amplitude.

Regarding the activity ranking of the pre-reduced catalysts, this can be followed best using their T_{50} behavior, as depicted in Figure 3c. Similar to that observed for the pre-oxidized samples (Figure 2c), an inverted volcano-type behavior of the activity with increasing substitutions (X) of La with Sr is once again clear (Figure 3c). Thus, LS_XM and Ir/LS_XM, when X = 0%, outperformed those when X = 30%, to a greater extent than those when X = 50% (the least active). Then, catalysts with X = 70% appeared more active than those with intermediate X values, approaching the optimal activity of those when X = 0%. Moreover, during the heating part of the light-off/light-out cycle, Ir/LS_XM catalysts appeared to exhibit a slightly superior performance compared with their LS_XM counterparts, except in the case of the $LS_{50}M$—$Ir/LS_{50}M$ pair (Figure 3c); these behaviors are almost opposite to those recorded for the pre-oxidized samples (Figure 2c). The same is true for the catalysts where X = 0 and 30% (low Sr content), but not for cases where X = 50% and 70% (high Sr content) during the cooling part of the cycle.

When comparing the behaviors of pre-reduced and pre-oxidized LSxM (Figure S5a) and Ir/LSXM (Figure S5b) catalysts, a clear trend is revealed; in the vast majority of cases, the cooling part of the pre-reduced catalysts better approximates, or even coincides with, the behavior of their pre-oxidized counterparts. A typical example (for the $Ir/LS_{30}M$ catalyst) is shown in Figure 3d.

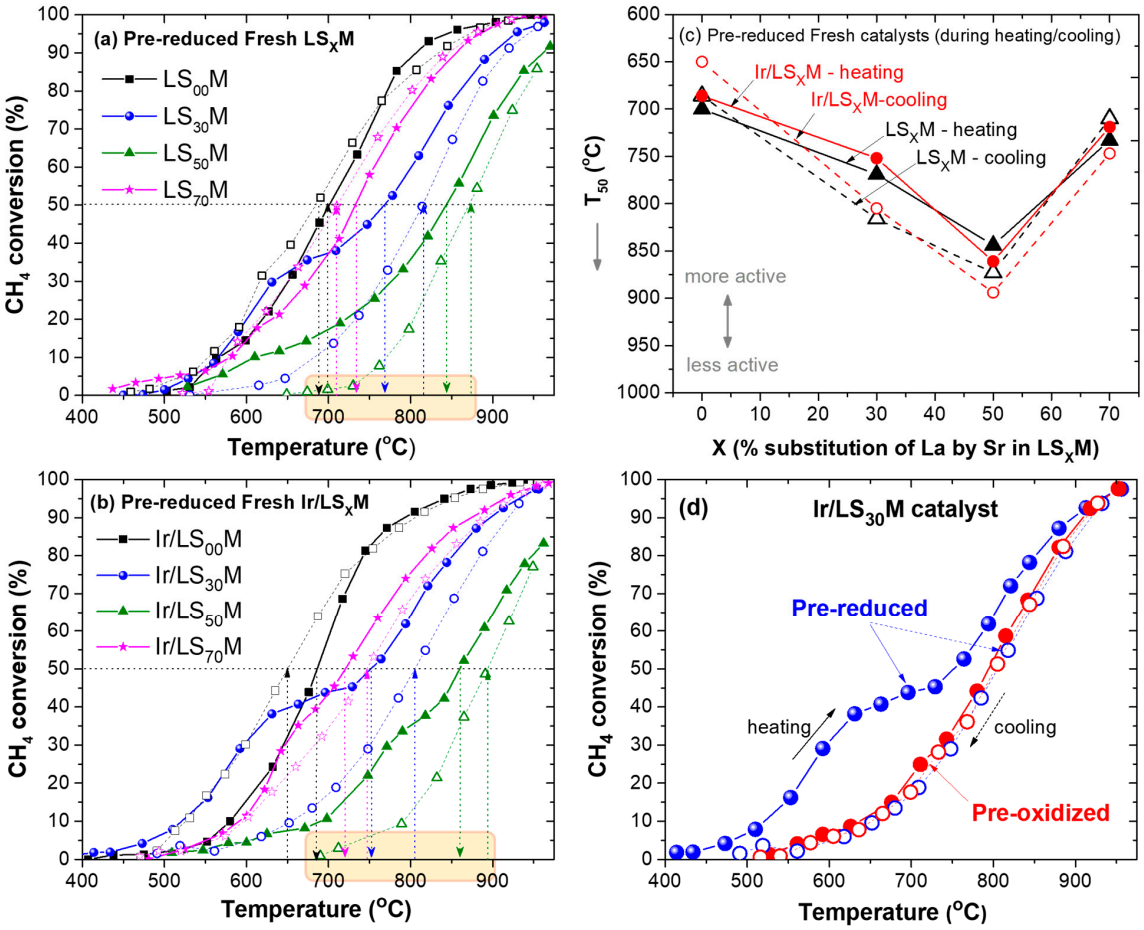

Figure 3. Light-off/light-out behavior of pre-reduced, fresh, LS_XM (**a**) and Ir/LS_XM (**b**) catalysts and the corresponding T_{50} values as a function of X (**c**). A selected comparison of the heating/cooling cycles obtained from the pre-reduced (blue symbols and lines) and pre-oxidized (red symbols and lines) $Ir/LS_{30}M$ catalysts (**d**). Feed conditions, as shown in Figure 2. Solid symbols and lines show the heating path of the cycles, open symbols and dashed lines show the cooling path of the cycles.

3.3. Light-Off/Light-Out Performance of LS_XM and Ir/LS_XM Catalysts Aged at 750 °C

Herein, the behavior of CH_4 conversion as a function of temperature during heating/cooling cycles between 400 and 900 °C is presented for LS_XM and Ir/LS_XM catalysts that were previously subjected to oxidative thermal aging for 5 h, as described in Scheme 1. Both the pre-oxidized and pre-reduced states of the samples at the beginning of the cycle were investigated.

3.3.1. Pre-Oxidized Catalysts Aged at 750 °C

Figure 4 presents the CH_4 conversion results obtained during the heating/cooling cycle for the pre-oxidized LS_XM (Figure 4a) and the Ir/LS_XM (Figure 4b) catalysts that were aged at 750°C, whereas Figure 4c depicts the corresponding T_{50} behavior of the catalysts as a function of X. As for fresh catalysts (Figure 2), no hysteresis phenomena were observed during the cycles over the pre-oxidized, aged at 750°C samples. It was also observed that pure perovskites (LS_XM) slightly outperformed their Ir-doped counterparts (Ir/LS_XM), except for $LS_{00}M$ (Figure 4c).

Regarding the dependence of the activity on the Sr content of LS_XM, the aged catalysts maintained the same behavior for their fresh counterparts (Figure 2). It is once again an inverted volcanic-type dependent activity competing against X, with $LS_{50}M$ and $Ir/LS_{50}M$ catalysts exhibiting inferior performances, with T_{50} values approximately 250 °C higher than those for $LS_{00}M$ and $Ir/LS_{00}M$ (Figure 4c).

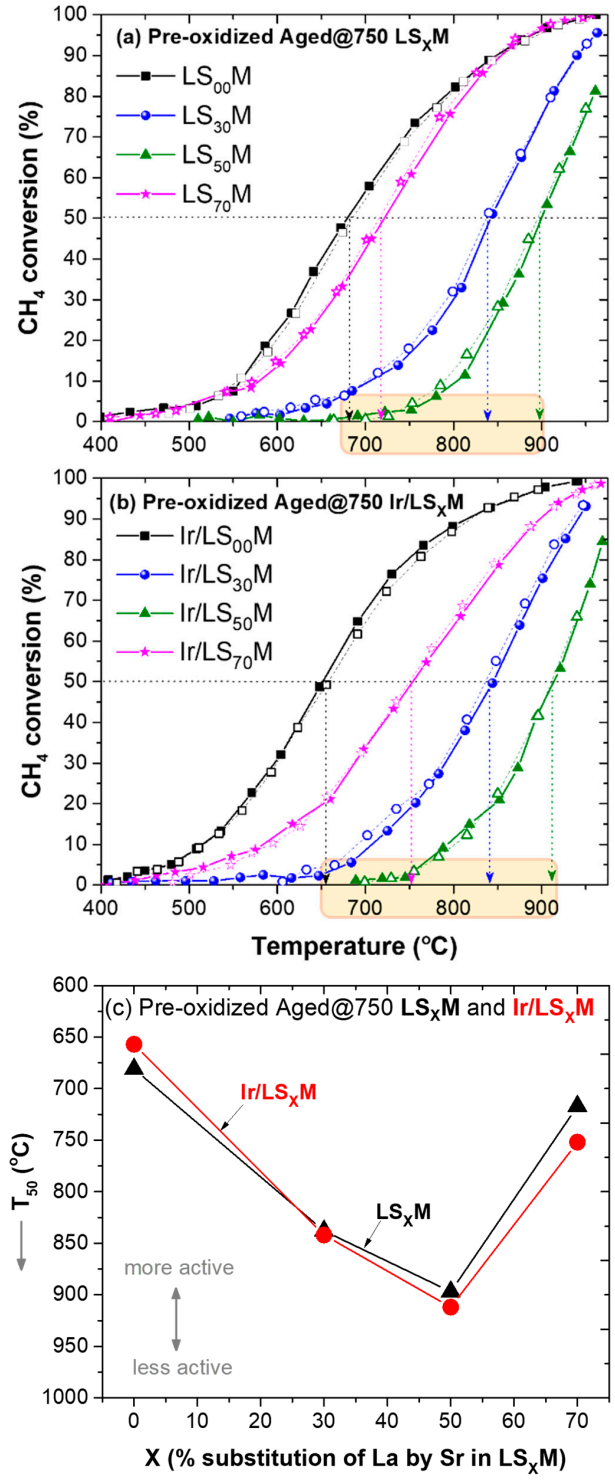

Figure 4. Light-off/light-out behavior of pre-oxidized, aged at 750 °C, LS_XM (**a**) and Ir/LS_XM (**b**) catalysts, and their corresponding T_{50} values as a function of X (**c**). Feed conditions are shown, as in Figure 2. Solid symbols and lines in (**a**,**b**) show the heating path and open symbols, and the dashed lines show the cooling path of the cycle.

3.3.2. Pre-Reduced Catalysts Aged at 750 °C

The performance of the pre-reduced LS_XM and Ir/LS_XM catalysts that were aged at 750 °C, and their impact on the lean CH_4 oxidation reaction during heating/cooling cycles, are depicted in Figure 5a,b, respectively. There are no significant differences compared with what was already observed in the behavior of their fresh counterparts. Again, hysteresis

phenomena, which are more pronounced for the intermediate values of the percentages where La was substituted for Sr (X = 30 and 50%), were observed.

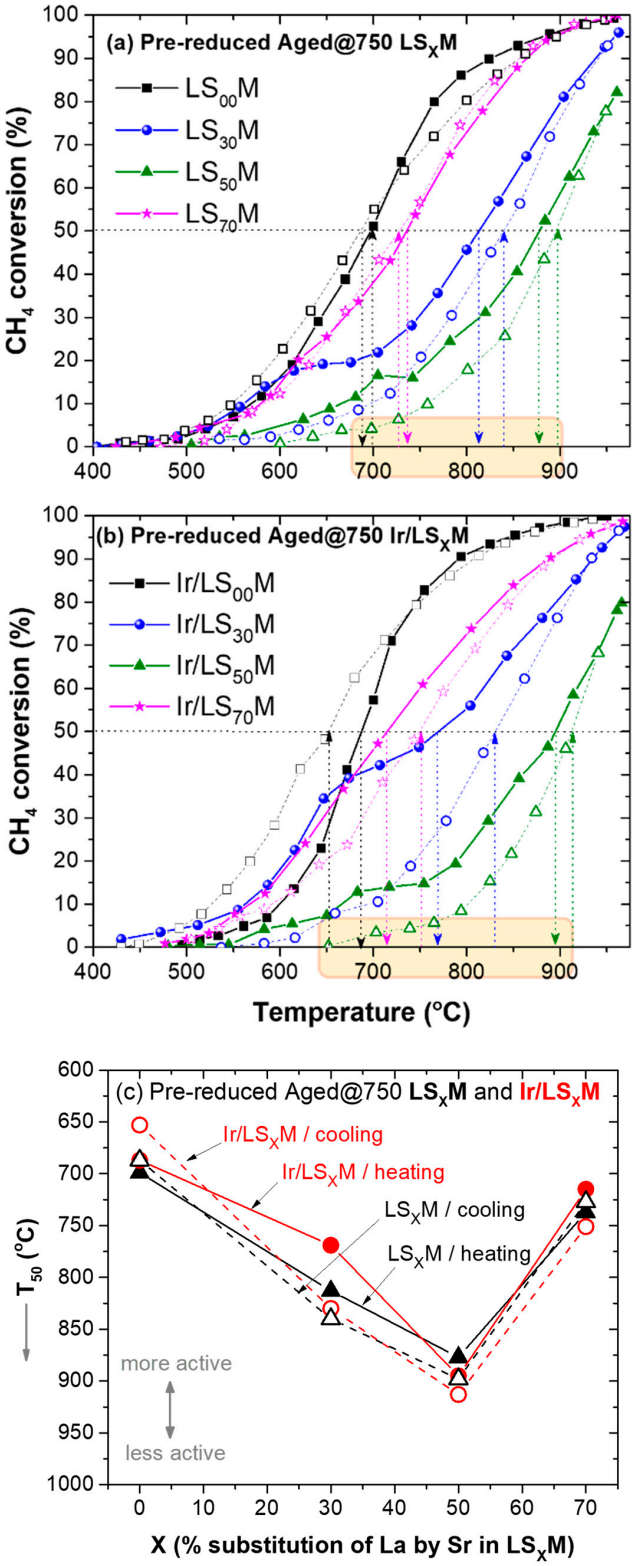

Figure 5. Light-off/light-out behavior of pre-reduced, aged at 750 °C, LS$_X$M (**a**) and Ir/LS$_X$M (**b**) catalysts, and their corresponding T$_{50}$ values as a function of X (**c**). Feed conditions are shown, as in Figures 2–4. Solid symbols and lines show the heating path, and open symbols and dashed lines show the cooling path of the cycle.

The CH_4 conversion efficiency performance versus X of the pre-reduced catalysts aged at 750 °C, in terms of T_{50}, is shown in Figure 5c. There are some variations in T_{50} values between the heating and cooling parts of the cycle due to the hysteresis, which generally indicates more active catalysts in the heating part of the loop. Since the thermal cycle starts with pre-reduced catalysts, it is possible that in this part of the cycle, the pre-imposed metallic Ir^0 is partially oxidized by the oxidizing environment of the reactants (lean conditions), creating an IrO_2/Ir^0 complex state. As demonstrated by Rui and co-workers [91], this offers favorable sites for the overall methane oxidation reaction, compared with metallic Ir^0 or stoichiometric IrO_2. In the same vein as the results of Schick et al. [31], regarding the total oxidation of VOCs over Ir/SiO_2 catalysts, which showed that surface Ir^{3+} species are associated with improved catalyst performance as well as size–activity relationship; regarding the latter, this is because as the size of the Ir nanoparticles decreases, the defective Ir^{3+} active sites increase.

However, when the system achieves 100% CH_4 conversion at a high temperature, i.e., it operates in net oxidizing conditions, (due to the remained unconsumed O_2, the Ir nanoparticles are fully oxidized into stoichiometric IrO_2, therefore, they become less active in the reaction, and during its return to low temperatures (cooling) the system exhibits lower activity.

Nevertheless, the effect of substituting La with Sr (X) remains the main cause of strong changes in terms of the efficiency of the catalysts. Changes in the order of ~60 °C max. were obtained between the heating and cooling sections of the hysteresis loop; these are insignificant compared with changes of 250 °C, caused by the 50% replacement of La with Sr.

3.4. Thermal Aging and Time-on-Stream Stability of Catalysts

In order to evaluate the thermal stability of the materials after prolonged exposure to thermal aging at high temperatures under oxidizing conditions (5 h at 750 °C in a 20% O_2/He flow), Figure 6 was constructed, which presents the efficiency (in terms of T_{50}) of fresh and aged (at 750 °C) LS_XM (Figure 6a–c) and Ir/LS_XM (Figure 6d–f) catalyst series.

For the pre-oxidized catalysts of each series, LS_XM and Ir/LS_XM, which do not show hysteresis after such a pretreatment, one diagram is sufficient for their comparison (Figure 6a for LS_XM and Figure 6d for Ir/LS_XM). However, for pre-reduced catalysts exhibiting hysteresis, a comparison is made with respect to both the heating and cooling parts of the hysteresis loops (Figure 6b,c for LS_XM and Figure 6e,f for Ir/LS_XM).

It is evident from Figure 6 that aging causes the degradation of the catalytic efficiency of the studied materials, but this is rather insignificant, as in most cases, this results in only slight increases in T_{50} (ca. +20 °C). Furthermore, in the case of catalysts with X = 0 and 70%, the activity of the catalysts, either of unloaded or Ir-loaded perovskites, remains unaffected after aging. The thermal aging stability of perovskites under oxidizing conditions is well established, and its confirmation it was not surprising to obtain this result for the pristine LSxM (Figure 6a–c). Moreover, the strong susceptibility and tendency to aggregate, regarding the supported iridium nanoparticles under oxidative thermal aging conditions, is also known [37,38], and thus, it was the focus of the stability experiments. However, the results of Figure 6d–f are similar to those of the pristine perovskites; the Ir/LS_XM catalysts exhibited good stability, and an explanation for this is given below.

Regarding the time-on-stream stability (TOS) of our catalysts, experiments were performed for a period of 12 h (Figure 7) under constant temperatures that corresponded with the T_{50} exhibited by each of them. The less active catalysts, $LS_{50}M$ and $Ir/LS_{50}M$, with high T_{50} values (~900 °C), were operated at temperatures of 850 °C; at such temperatures, they have an initial CH_4 conversion rate of about 20–25% (Figure 7). All catalysts showed very good stability, since only a slight degradation, in the order of 5%, was recorded after 12 h of operation. It is worth noting that the catalyst pair, $LS_{00}M$ and $Ir/LS_{00}M$, was the most active compared with all others investigated, and it also offered the best TOS stability, with zero degradation in terms of their efficiency, over the 12 h period.

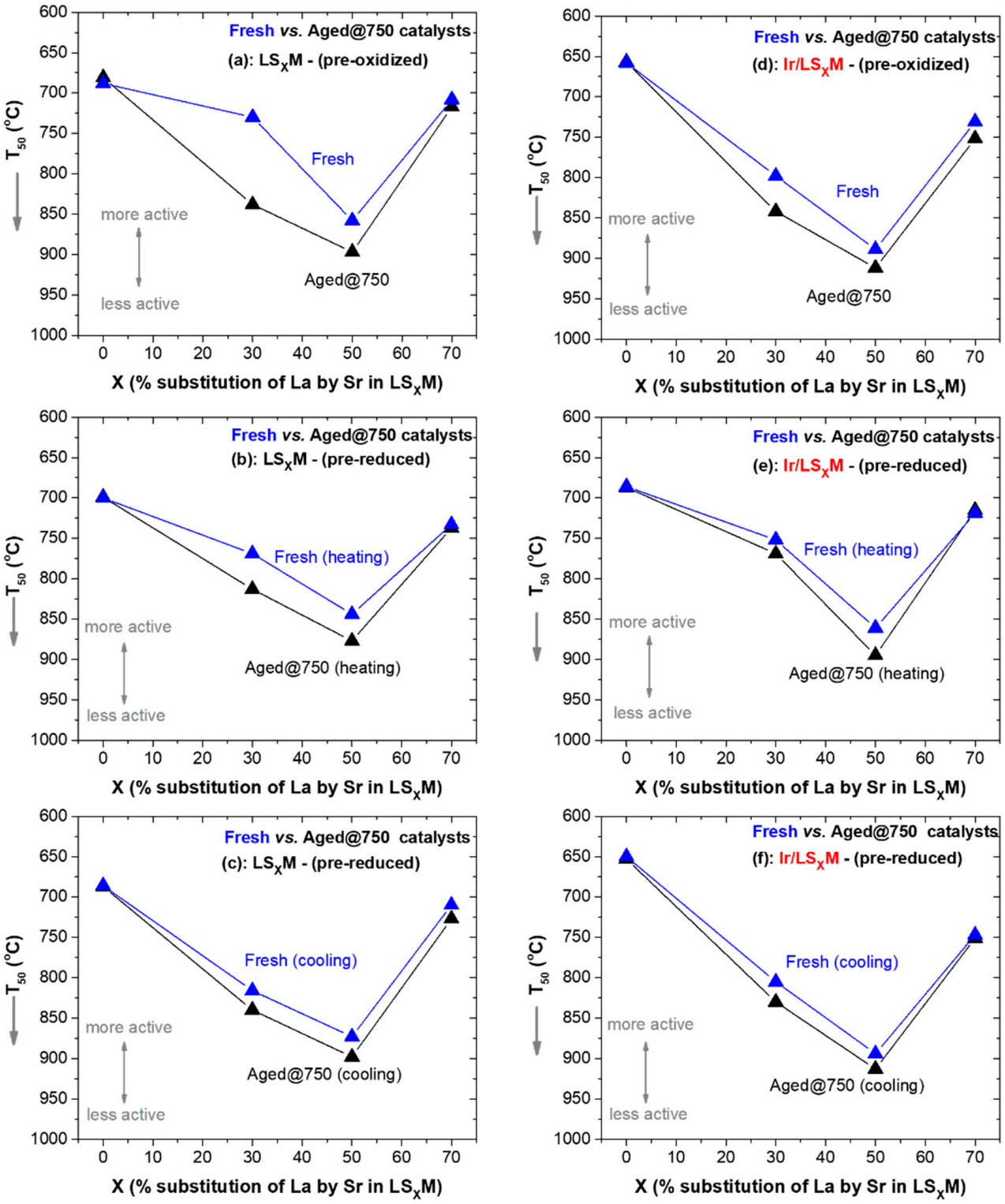

Figure 6. Comparison of fresh and aged at 750 °C LS_XM and Ir/LS_XM catalysts in T_{50} vs. X diagrams. (**a**–**c**) correspond with LS_XM; (**d**–**f**) correspond with Ir/LS_XM. (**a**,**d**) compare fresh vs. aged (at 750 °C) pre-oxidized LS_XM and Ir/LS_XM catalysts, respectively; (**b**,**c**) compare fresh vs. aged (at 750 °C) pre-reduced LS_XM and Ir/LS_XM catalysts during heating, respectively; (**c**,**f**) compare fresh vs. aged (at 750 °C) pre-reduced LS_XM and Ir/LS_XM catalysts during cooling, respectively. Feed conditions are shown, as in Figures 2–5.

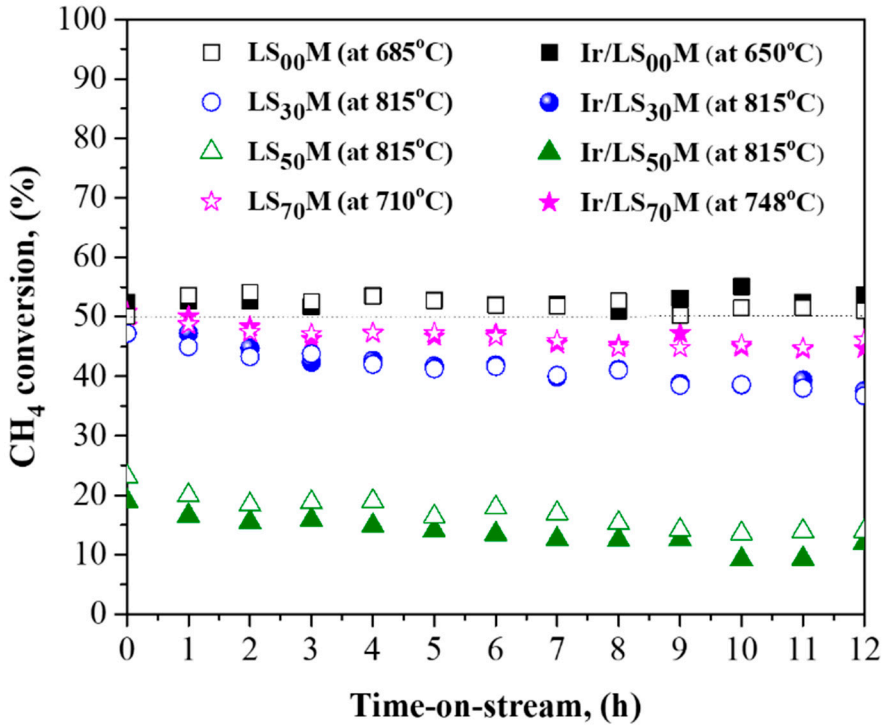

Figure 7. A 12 h time-on-stream stability test for the LS_XM (open symbols) and Ir/LS_XM (closed symbols) catalysts. Conditions: 1.0% CH_4 + 5.0% O_2, He balance at 1 atm, F_T = 75 mL/min, m_{cat} = 50 mg, WGHSV = 90,000 mL/g·h. Regarding the temperature (indicated in figure inset), it was close to T_{50} for each catalyst, except for the less active pair, $LS_{50}M$ and $Ir/LS_{50}M$.

3.5. Main Observations and Material Properties—Catalytic Efficiency Correlations

The main observations of the above comparative studies of catalytic behavior (efficiency and stability) of the two series of LS_XM and Ir/LS_XM catalysts for the complete CH_4 oxidation reaction under lean conditions, can be summarized as follows:

(i) The most important determining factor of the materials, for all cases (unloaded or Ir-loaded LS_XM, pre-oxidized or pre-reduced, and fresh or aged materials), in terms of efficiency, was the composition of the LS_XM perovskite, specifically, the amount of La that was substituted with Sr (X = 0, 30, 50, and 70%). This key factor typically causes shifts in T_{50} of up to ca. 300 °C, whereas other parameters appeared capable of shifts in T_{50} that were one order of magnitude lower (ca. 30 °C) (Figures 2–5).

(ii) X variation produced an inverted volcanic-type effect in terms of catalytic efficiency, with the most active in all cases the catalysts that did not contain Sr, i.e., X = 0% ($LS_{00}M$ = $LaMnO_3$ and $Ir/LS_{00}M$ = $Ir/LaMnO_3$), and less active the catalysts with X = 50% (i.e., $LS_{50}M$ and $Ir/LS_{50}M$). Catalysts with larger X value (X = 70%; $La_{0.3}Sr_{0.7}MnO_3$ and $Ir/La_{0.3}Sr_{0.7}MnO_3$), tended to be similar to the behavior of the optimal catalysts ($LaMnO_3$ and $Ir/LaMnO_3$) (Figures 2c–5c and 6).

(iii) The addition of Ir nanoparticles onto the LS_XM surface did not perform as expected. It had a negative effect on the efficiency of pre-oxidized catalysts (Ir/LS_XM show T_{50} values that were ~30°C higher than those of their non-loaded LS_XM counterparts) (Figures 2c and 4c), whereas the pre-reduced catalysts exhibited a small positive effect at high temperatures, but it was more noticeable for lower temperatures (Figures 3c and 5c).

(iv) Hysteresis phenomena during heating/cooling cycles appeared only in the case of pre-reduced catalysts for both LS_XM and Ir/LS_XM series (Figures 3 and 5), whereas for pre-oxidized materials, the light-off and light-out curves faithfully coincided with each other (Figures 2 and 4).

(v) The hysteresis loops are qualitatively similar for the corresponding LS_XM and Ir/LS_XM catalysts, which indicates that the phenomenon is mainly determined by LS_XM and its properties, rather than Ir (Figures 3 and 5).

(vi) The oxidative thermal aging of the materials caused marginal decreases in their efficiency (i.e., less than ~40 °C shifts of T_{50} towards higher temperatures). However, for the most active catalysts (with X = 0 and 70%), no activity deterioration was recorded (Figure 6).

(vii) The time-on-stream stability of the materials was generally good, as the efficiency (methane conversion) only declined by 5–10%; this was observed after 12 h of operation. Notably, no degradation in the catalytic efficiency of the optimal $LS_{00}M$ ($LaMnO_3$) and $Ir/LS_{00}M$ ($Ir/LaMnO_3$) catalysts was recorded (Figure 7).

After a close comparison of the LS_XM characteristics (and how these change in accordance with the extent (X) to which La was substituted with Sr) with the catalytic results, we can readily conclude that the main factors affecting the activity of the perovskites during the lean CH_4 combustion are the total surface area (S_{BET}) and the reducibility of the perovskite. Indeed, as shown in Figure 8a and b, respectively, the efficiency of the LS_XM (in terms of T_{50}) faithfully mimics the changes in both the total surface area (S_{BET}) and reducibility (expressed in terms of the peak temperature of $Mn^{4+} \rightarrow Mn^{3+}$ reduction in the TPR profile of Figure 1) when the level of substituted Sr (X) in the perovskite increases.

Studies of the literature, regarding lean CH_4 combustion over perovskite-type materials, typically describe the reaction mechanism via the Eley–Rideal (ER), Mars–van Krevelen (MVK), and/or both (two-term) kinetic models [63,67,79]. The ER model involves the direct reaction of gas phase methane with adsorbed oxygen species (O_{ads}) on the perovskite surface. The MVK model implicates the reaction of gas phase CH_4 with surface lattice oxygen (Equation (6)), the latter being continuously replenished by the dissociative chemisorption of O_2 on surface oxygen vacancies (Equation (7)), as follows:

$$4O_O^{\times} + CH_4 \rightarrow CO_2 + 2H_2O \quad (6)$$

$$\frac{1}{2}O_2(g) \Leftrightarrow O_O^{\times} \quad (7)$$

Performing Density Functional Theory (DFT) calculations for CH_4 combustion on LSM perovskites, Wang et al. [92] also indicated that CH_4 adsorption and activation ($CH_4^* \rightarrow CH_3^* + H^*$) occurs on Mn sites. They argued that this activation, revealed to be more facile on the (001) rather than (110) crystallographic plane, can cause further enhancements to catalytic methane oxidation after a reaction concerning such methane-derived species with neighbor lattice oxygen atoms takes place.

It is therefore obvious from the above considerations that perovskite activity, regarding the reaction under consideration, will be directly proportional to the population of labile oxygen species on the perovskite surface, and thus, to the perovskite surface area itself. At the same time, the degree of lability of these lattice oxygen species would act synergistically upon the enhancement of the activity.

Observations (i) and (ii) that are related to the entire catalytic efficiency data, either obtained on fresh or aged, or on pre-oxidized or pre-reduced, catalysts, they exhibit an activity order ($LS_{00}M \sim LS_{70}M > LS_{30}M > LS_{50}M$) that is fully consistent with the above. The higher the perovskite surface area and lattice oxygen lability, the higher its efficiency in terms of lean CH_4 combustion (Figure 8c,d). As we have seen here, increasing the amount of substituted Sr in LS_XM, up to X = 50%, gradually degrades both of these activity-determining parameters; for X = 70%, however, the formation of other simple oxide phases (e.g., Mn_2O_3, see XRD results in Figure S2) may be the cause of the recovery of high values in said properties, and therefore, the return of efficiency to high values.

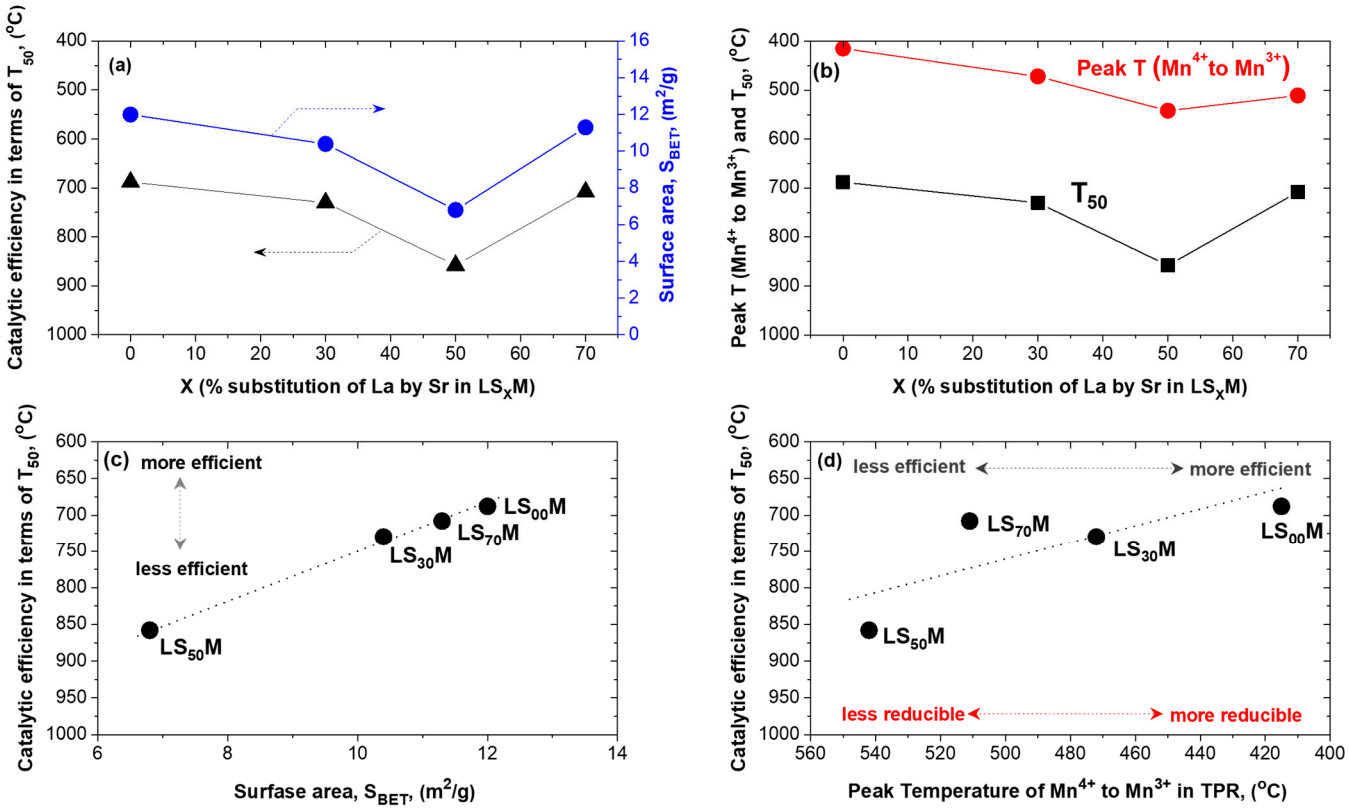

Figure 8. Correlations between the LS_XM lean CH_4 combustion efficiency and its textural characteristics and properties, which were mainly changed as a result of the degree of Sr substitution (X). (**a**) Variation in LS_XM surface area and efficiency (T_{50}) as a function of X; (**b**) variation of LS_XM reducibility (in terms of peak temperature of the $Mn^{4+} \rightarrow Mn^{3+}$ reduction in the TPR profile) and efficiency (T_{50}) as a function of X; (**c**) direct correlation of LS_XM catalytic efficiency with its surface area; and (**d**) direct correlation of LS_XM catalytic efficiency with its reducibility.

The unexpected inhibitory effect of adding Ir to the surface of LS_XM perovskites, regarding their catalytic efficiency (observation iii), is still uncertain. As shown in Table 1, the Ir/LS_XM catalysts typically have a lower surface area compared with their LS_XM counterparts due to their partially blocked pores, as explained in Section 3.1. Therefore, part of the surface of the perovskite support, which is intrinsically active in the reaction, is rendered inaccessible to the reactants mixture. The catalyst thus loses active centers, which, in the case of pre-oxidized samples, are not replenished by the presence of, relatively inactive to the reaction, IrO_2 phase. In the case of the pre-reduced Ir/LS_XM catalysts, this undesirable effect of the iridium species is partially compensated with the creation of an active for the reaction IrO_2/Ir^0 phase (partially oxidized iridium) [31,91]. This occurs after the exposure of the Ir^0 species of the pre-reduced catalysts to the excess O_2 conditions. However, as our results show, this favorable partially oxidized surface of the iridium particles (IrO_2/Ir^0) created on the pre-reduced catalysts is not expected to remain in high temperatures and under excess O_2 reaction conditions. It transforms to the less active IrO_2 which moderates positive effects (Figures 3 and 5).

The consistent interpretations of observations (iv) and (v), which are related to inverse hysteresis phenomena (Figures 3 and 5), and are recorded in this study, are as follows:

Why is hysteresis observed only on the pre-reduced, and not the pre-oxidized, catalysts, and why is it of the inverse type (i.e., clockwise, the heating part outperforms its cooling part)? The light-off (heating part) behavior of the pre-reduced catalysts (Figures 3 and 5) is very similar to the behavior first observed by Arai et al. [67], who studied CH_4 combustion on $La_{0.8}Sr_{0.2}MnO_3$ and $La_{0.6}Sr_{0.4}MnO_3$ perovskites using a reaction mixture of 2% v/v CH_4 in air. It exhibits a characteristic "hump" in the low-temperature region, then,

it changed curvature at higher temperatures, as also found herein (Figures 3 and 5). We agree with the explanation given by the authors, as follows. The initial high rate of CH_4 consumption is the result of the contribution to the overall rate of adsorbed oxygen species (O_{ads}) on the perovskite surface which is then limited by increasing temperatures (at high temperatures the O_{ads} desorb rapidly); however, at high temperatures the participation of lattice oxygen ($O_O^{\times}$) in methane oxidation becomes dominant [67].

Regarding the behavior of the cooling (light-out) part of the hysteresis loops (Figures 3 and 5), we can give the following rational explanation. When approaching ~100% methane conversion at the upper-temperature limit, the catalyst experiences pure oxidative conditions (~100% CH_4 conversion, excess O_2). It is therefore oxidized under such conditions, and by lowering the temperature, it follows a path of lower activity, similar to the results obtained in pre-oxidized samples (Figures 2 and 4). This explains why the cooling part of the hysteresis loops was always similar to the light-off curves of the pre-oxidized catalysts, in addition to the "inverse" character of the hysteresis.

In accordance with the above, hysteresis mainly occurs due to the favorable contribution of O_{ads} species to the total methane consumption rate. However, the reason why this was found to only work for pre-reduced samples, but not pre-oxidized samples, can be interpreted as follows. The pre-reduction process of LSxM materials is expected to enhance the population of oxygen vacancies on their surface due to a partial $Mn^{4+} \rightarrow Mn^{3+}$ reduction. When such a pre-treated LS_XM perovskite experiences in methane oxidation environments, the gas phase dioxygen interacts with oxygen vacancies, providing two atomic oxygens, one of which is bound by the vacancy that becomes the lattice oxygen, and the other can diffuse to the perovskite surface in the form of adsorbed O_{ads}. Thus, a mechanism of continuous replacement concerning both lattice and adsorbed oxygen species is at work during the reaction on pre-reduced materials. Conversely, the pre-oxidized perovskites, due to the lack of oxygen vacancies on their surface to activate the dissociative chemisorption of gaseous dioxygen in this temperature range, have a limited amount of O_{ads} that impose low reaction rates. Thus, for per-oxidized samples, both the heating and cooling parts of the light-off experiments coincide since the samples work for both paths in their oxidized state.

The presence of Ir in the catalyst formulations (Ir/LS_XM) appears to have some noticeable effect on the hysteresis phenomena, especially on loop amplitude, regarding CH_4 conversion. It appears strongly enlarged (Figure 5b) compared with that recorded in the corresponding LS_XM catalysts (Figure 5a). A reasonable explanation is that the partially oxidized IrO_2/Ir^0 sites (their creation has been described above), which are favorable for the dissociative adsorption of gaseous dioxygen, further facilitate this necessary mechanistic step of the reaction. The as-derived oxygen atoms can then directly react with the methane, and/or spillover to the perovskite surface, thus replenishing the lattice oxygen consumed by the reaction, enhancing methane combustion.

Regarding observation (vi), which concerns the good stability of our materials in spite of the fact that they were subjected to arduous conditions, even those containing Ir (Ir/LS_XM), is an impressive finding considering that Ir is a very sensitive catalyst with regard to thermal aging; it has a high aggregation tendency, even at temperatures as low as 450°C [13,14,37–41]. The present results once again confirm our recent experimental findings, theory, and developed model, demonstrating that supports possess a sufficient population of bulk and surface O-defects (oxygen vacancies), and a high mobility of lattice O^{2-} ions effectively act against the thermal sintering of catalyst nanoparticles dispersed on their surface [40,41]. The perovskites used herein as supports for Ir nanoparticles meet these requirements.

Observation (vii), on the other hand, concerning the good time-on-stream stability of our materials, most likely reflects the absence of the accumulative carbon deposition phenomena originating from the methane cracking reaction, the occurrence of which is not thermodynamically excluded in the temperature range used for the reaction in this study.

An additional aspect worth noting in the present findings concerns the fact that, in the literature, it is known that at high temperatures (ca. > 850 °C, reached in the present study) the contribution of the gas phase to the total methane oxidation can be appreciable under certain conditions and should not be ignored. Matzaras and co-workers, in a Cartesian plot of SV (surface-to-volume ratio) versus residence time, delineated the regimes concerning the significant involvement of gas-phase chemistry for given pressures and temperatures [93]. Considering the conditions in which the present experiments were performed (SV > 200,000 and residence time ~0.017 s at a pressure of 1 bar), it seems that the catalytic system operates under conditions that starkly differ with those wherein the contribution of the gas-phase reaction could be noticeable. This view is further strengthened by two additional facts, as follows: first, no slope change tendency of the light-off curves at high temperatures is observed in Figures 2–5; second, nor was CO detected in the reaction products (the contribution of the gas phase goes through the reaction sequence: $CH_4 \rightarrow$ CO gas-phase route followed by the catalytic oxidation of the produced gaseous CO to CO_2).

Finally, taking into account the small particle size of the catalytic powdered samples (180–250 μm), and the high GHSV used (ca. 156,000 h^{-1}), mass and heat transfer limitations, if any, should be negligible.

4. Conclusions

The complete oxidation of the methane reaction was investigated in detail on a series of LS_XM (X = % substitution of La with Sr = 0, 30, 50, and 70%) perovskites, and on their 2 wt% Ir-loaded counterpart catalysts.

The key parameter affecting efficiency for both series concerned the degree (X) of substitutional Sr, rather than the addition of Ir; the latter caused a slight inhibition of activity, rather than promotion, when in its oxidation state (IrO_2), and it notably enhanced activity when in a partially oxidized state (IrO_2/Ir^0).

The main factors through which parameter X affects the activity were the changes it induced in the materials' total surface area and on their reducibility that act synergistically.

The materials' efficiency followed an inverted volcanic behavior pattern, as a function of X, with the most efficient catalysts being the $LS_{00}M$—$Ir/LS_{00}M$ pair, and the least efficient being the $LS_{50}M$—$Ir/LS_{50}M$ pair; this strikingly reflects the effect of X on the total surface area and the reducibility of the materials. Large differences in T_{50} (ca. 300 °C) were recorded between the most and least active catalysts.

The inhibitory effect on efficiency, caused by the addition of Ir to the perovskite, was attributed to partial pore blocking, and consequently, to a reduction in the number of active sites, in combination (for pre-oxidized catalysts) with the low activity of IrO_2 particles. For pre-reduced catalysts, the creation under reaction conditions of a reactive partially oxidized IrO_2/Ir^0 phase enhanced activity, especially at low temperatures.

Inverse hysteresis phenomena recorded on pre-reduced, but not pre-oxidized, LSxM and Ir/LS_XM catalysts during light-off (heating)/light-out (cooling) temperature cycles and overall reaction kinetics were consistently interpreted by assuming that CH_4 oxidation was performed in parallel with O_{ads} species (Eley–Rideal model) and lattice oxygens (Mars–van Krevelen model) (i.e., a two-term kinetic model).

Both the LS_XM and Ir/LS_XM series of materials were found to be very stable in both oxidative thermal aging tests at 750 °C for 5 h, and the 12 h time-on-stream stability tests under the reaction's conditions.

The great stability of perovskites at high temperatures for the total oxidation of CH_4, the convenience they provide for effectively tailoring their performance via the partial substitution of the A or B sites with other cations, and the efficient CH_4 conversion they achieve, even without noble metal loading, make them promising materials that are worthy for future studies concerning demanding applications such as exhaust gas treatment in NG-driven vehicles or gas turbines (GTs).

Supplementary Materials: The following supporting information can be downloaded at: https://www.mdpi.com/article/10.3390/nano13152271/s1: Figure S1. Schematic configuration of the continuous flow experimental apparatus equipped with on-line Gas Chromatography; Figure S2. XRD patterns of LS_XM perovskites ($La_{1-x}Sr_xMnO_3$; X = 0, 30, 50 and 70% substitution of La by Sr) and the corresponding 2 wt% Ir/LS_XM catalysts; Figure S3. Magnification of the XRD patterns of LS_XM perovskites at the region 2θ = 32–34°, where the main peak of the perovskite phase appears; Figure S4. H_2 consumption versus temperature (H_2-TPR profiles) of Ir/LS_XM catalysts. Figure S5. Dependence of T_{50} on X (% substitution of La by Sr in the perovskite composition) for pre-reduced and pre-oxidized LS_XM catalysts (a), and pre-reduced and pre-oxidized Ir/LS_XM catalysts (b); Table S1. Temperature for 50% CH_4 conversion (T_{50}) of pre-oxidized and pre-reduced, fresh LS_XM and Ir/LS_XM catalysts; Table S2. Temperature for 50% CH_4 conversion (T_{50}) of pre-reduced and pre-oxidized LSxM and Ir/LSxM catalysts that were aged at 750 °C.

Author Contributions: Conceptualization, C.D. and I.V.Y.; methodology, C.D. and I.V.Y.; validation, C.D., I.V.Y. and V.T.Z.; formal analysis, C.D., I.V.Y. and E.N.; investigation, C.D., E.N., T.G. and S.F.; resources, I.V.Y.; data curation, C.D., E.N. and S.F.; writing—original draft preparation, I.V.Y.; writing—review and editing, I.V.Y., C.D., E.N. and V.T.Z.; visualization, C.D. and I.V.Y.; supervision, I.V.Y.; project administration, I.V.Y.; funding acquisition, I.V.Y. All authors have read and agreed to the published version of the manuscript.

Funding: This research has been co-financed by the European Union and Greek national funds under the call "Greece–China Call for Proposals for Joint RT&D Projects" (Project code: T7DKI-00356).

Data Availability Statement: The data are available from the laboratory of origin upon request www.pccplab.tuc.gr (accessed on 1 March 2023).

Conflicts of Interest: The authors declare no conflict of interest.

References

1. Zhang, X.; Myhrvold, N.P.; Hausfather, Z.; Caldeira, K. Climate benefits of natural gas as a bridge fuel and potential delay of near-zero energy systems. *Appl. Energy* **2016**, *167*, 317–322. [CrossRef]
2. Brauers, H. Natural gas as a barrier to sustainability transitions? A systematic mapping of the risks and challenges. *Energy Res. Soc. Sci.* **2022**, *89*, 102538. [CrossRef]
3. Weissman, S. Natural Gas as a Bridge Fuel. Measuring the Bridge. Center for Sustainable Energy. Available online: https://energycenter.org/sites/default/files/docs/nav/policy/research-and-reports/Natural_Gas_Bridge_Fuel.pdf (accessed on 9 February 2023).
4. Jiang, D.; Khivantsev, K.; Wang, Y. Low-Temperature Methane Oxidation for Efficient Emission Control in Natural Gas Vehicles: Pd and Beyond. *ACS Catal.* **2020**, *10*, 14304–14314. [CrossRef]
5. Stoian, M.; Roge, V.; Lazar, L.; Maurer, T.; Vedrine, J.C.; Marcu, I.-C.; Fechete, I. Total Oxidation of Methane on Oxide and Mixed Oxide Ceria-Containing Catalysts. *Catalysts* **2021**, *11*, 427. [CrossRef]
6. Yentekakis, I.V.; Goula, G. Biogas management: Advanced utilization for production of renewable energy and added-value chemicals. *Front. Environ. Sci.* **2017**, *5*, 7. [CrossRef]
7. Jiang, Y.; Yentekakis, I.V.; Vayenas, C.G. Methane to ethylene with 85 percent yield in a gas recycle electrocatalytic reactor-separator. *Science* **1994**, *264*, 1563–1566. [CrossRef]
8. Siakavelas, G.I.; Charisiou, N.D.; AlKhoori, A.; Sebestian, V.; Hinder, S.J.; Baker, M.A.; Yentekakis, I.V.; Polychronopoulou, K.; Goula, M.A. Cerium oxide catalysts for oxidative coupling of methane reaction: Effect of lithium, samarium and lanthanum dopants. *J. Environ. Chem. Eng.* **2022**, *10*, 107259. [CrossRef]
9. Yentekakis, I.V.; Dong, F. Grand Challenges for Catalytic Remediation in Environmental and Energy Applications Toward a Cleaner and Sustainable Future. *Front. Environ. Chem.* **2020**, *1*, 5. [CrossRef]
10. Yentekakis, I.V.; Panagiotopoulou, P.; Artemakis, G. A review of recent efforts to promote dry reforming of methane (DRM) to syngas production via bimetallic catalyst formulations. *Appl. Catal. B Environ.* **2021**, *296*, 120210. [CrossRef]
11. Osazuwa, O.U.; Abidin, S.Z.; Fan, X.; Amenaghawon, A.N.; Azizan, M.T. An insight into the effects of synthesis methods on catalysts properties for methane reforming. *J. Environ. Chem. Eng.* **2021**, *9*, 105052. [CrossRef]
12. Karam, L.; El Hassan, N. Advantages of mesoporous silica based catalysts in methane reforming by CO_2 from kinetic perspective. *J. Environ. Chem. Eng.* **2018**, *6*, 4289–4297. [CrossRef]
13. Yentekakis, I.V.; Goula, G.; Hatzisymeon, M.; Betsi-Argyropoulou, I.; Botzolaki, G.; Kousi, K.; Kondarides, D.I.; Taylor, M.J.; Parlett, C.M.A.; Osatiashtiani, A.; et al. Effect of support oxygen storage capacity on the catalytic performance of Rh nanoparticles for CO_2 reforming of methane. *Appl. Catal. B Environ.* **2019**, *24*, 490–501. [CrossRef]

14. Yentekakis, I.V.; Goula, G.; Panagiotopoulou, P.; Katsoni, A.; Diamadopoulos, E.; Mantzavinos, D.; Delimitis, A. Dry reforming of methane: Catalytic performance and stability of Ir catalysts supported on γ-Al_2O_3, $Zr_{0.92}Y_{0.08}O_{2-\delta}$ (YSZ) or $Ce_{0.9}Gd_{0.1}O_{2-\delta}$ (GDC) supports. *Top. Catal.* **2015**, *58*, 1228–1241. [CrossRef]
15. Nikolaraki, E.; Goula, G.; Panagiotopoulou, P.; Taylor, M.J.; Kousi, K.; Kyriakou, G.; Kondarides, D.I.; Lambert, R.M.; Yentekakis, I.V. Support Induced Effects on the Ir Nanoparticles Activity, Selectivity and Stability Performance under CO_2 Reforming of Methane. *Nanomaterials* **2021**, *11*, 2880. [CrossRef]
16. Barelli, L.; Ottaviano, A. Solid oxide fuel cell technology coupled with methane dry reforming: A viable option for high efficiency plant with reduced CO_2 emissions. *Energy* **2014**, *71*, 118–129. [CrossRef]
17. Gur, T.M. Comprehensive review of methane conversion in solid oxide fuel cells: Prospects for efficient electricity generation from natural gas. *Progr. Energy Combust. Sci.* **2016**, *54*, 1–64. [CrossRef]
18. Sengodan, S.; Lan, R.; Humphreys, J.; Du, D.; Xu, W.; Wang, H.; Tao, S. Advances in reforming and partial oxidation of hydrocarbons for hydrogen production and fuel cell applications. *Renew. Sustain. Energy Rev.* **2018**, *82*, 761–780. [CrossRef]
19. Yentekakis, I.V.; Papadam, T.; Goula, G. Electricity production from wastewater treatment via a novel biogas-SOFC aided process. *Solid State Ion.* **2008**, *179*, 15211525. [CrossRef]
20. Yentekakis, I.V. Open- and closed-circuit study of an intermediate temperature SOFC directly fueled with simulated biogas mixtures. *J. Power Sources* **2006**, *160*, 422–425. [CrossRef]
21. Miniajluk, N.; Trawczynski, J.; Zawadzki, M.; Tylus, W. $LaMnO_3$ ($La_{0.8}Sr_{0.2}MnO_3$) Perovskites for Lean Methane Combustion: Effect of Synthesis Method. *Adv. Mater. Phys. Chem.* **2018**, *8*, 193–215. Available online: http://creativecommons.org/licenses/by/4.0/ (accessed on 1 May 2023).
22. Gelin, P.; Primet, M. Complete oxidation of methane at low temperature over noble metal based catalysts: A review. *Appl. Catal. B Environ.* **2002**, *39*, 1–37. [CrossRef]
23. Li, H.; Fu, R.; Duan, W.; Jiang, Z. The preparation effect on activity and thermal stability of $La_{0.8}Ca_{0.2}FeO_3$ perovskite honeycombs dispersed by $MgAl_2O_4$ spinel washcoat for catalytic combustion of dilute methane. *J. Environ. Chem. Eng.* **2006**, *4*, 2187–2195. [CrossRef]
24. Chen, J.; Zhong, J.; Wu, Y.; Hu, W.; Qu, P.; Xiao, X.; Zhang, G.; Liu, X.; Jiao, Y.; Zhong, L.; et al. Particle Size Effects in Stoichiometric Methane Combustion: Structure–Activity Relationship of Pd Catalyst Supported on Gamma-Alumina. *ACS Catal.* **2020**, *10*, 10339–10349. [CrossRef]
25. Cimino, S.; Lisi, L.; Pirone, R.; Russo, G.; Turco, M. Methane combustion on perovskites-based structured catalysts. *Catal. Today* **2000**, *59*, 19–31. [CrossRef]
26. Gao, Y.; Jiang, M.; Yang, L.; Li, Z.; Tian, F.-X.; He, Y. Recent progress of catalytic methane combustion over transition metal oxide catalysts. *Front. Chem.* **2022**, *10*, 959442. [CrossRef]
27. Zhang, X.; Long, E.; Li, Y.; Guo, J.; Zhang, L.; Gong, M.; Wang, M.; Chen, Y. CeO_2-ZrO_2-La_2O_3-Al_2O_3 composite oxide and its supported palladium catalyst for the treatment of exhaust of natural gas engined vehicles. *J. Nat. Gas Chem.* **2009**, *18*, 139–144. [CrossRef]
28. Mortensen, R.L.; Noack, H.-D.; Pedersen, K.; Mossin, S.; Mielby, J. Recent Advances in Complete Methane Oxidation using Zeolite-Supported Metal Nanoparticle Catalysts. *ChemCatChem* **2022**, *14*, e202101924. [CrossRef]
29. Santos, V.P.; Carabineiro, S.A.C.; Tavares, P.B.; Pereira, M.F.R.; Orfao, J.J.M.; Figueirdo, J.L. Oxidation of CO, ethanol and toluene over TiO_2 supported noble metal catalysts. *Appl. Catal. B Environ.* **2010**, *99*, 198–205. [CrossRef]
30. Drosou, C.; Nikolaraki, E.; Nikolaou, V.; Koilia, E.; Artemakis, G.; Stratakis, A.; Evdou, A.; Charisiou, N.D.; Goula, M.A.; Zaspalis, V.; et al. Activity and Thermal Aging Stability of $La_{1-x}Sr_xMnO_3$ (x = 0.0, 0.3, 0.5, 0.7) and Ir/$La_{1-x}Sr_xMnO_3$ Catalysts for CO Oxidation with Excess O_2. *Nanomaterials* **2023**, *13*, 663. [CrossRef]
31. Schick, L.; Sanchis, R.; Gonzalez-Alfaro, V.; Agouram, S.; Lopez, J.M.; Torrente-Murciano, L.; Garcia, T.; Solsona, B. Size-activity relationship of iridium particles supported on silica for the total oxidation of volatile organic compounds (VOCs). *Chem. Eng. J.* **2019**, *366*, 100–111. [CrossRef]
32. Pachatouridou, E.; Papista, E.; Iliopoulou, E.F.; Delimitis, A.; Goula, G.; Yentekakis, I.V.; Marnellos, G.E.; Konsolakis, M. Nitrous oxide decomposition over Al_2O_3 supported noble metals (Pt, Pd, Ir): Effect of metal loading and feed composition. *J. Environ. Chem. Eng.* **2015**, *3*, 815–821. [CrossRef]
33. Yentekakis, I.V.; Goula, G.; Kampouri, S.; Betsi-Argyropoulou, I.; Panagiotopoulou, P.; Taylor, M.J.; Kyriakou, G.; Lambert, R.M. Ir-catalyzed nitrous oxide (N_2O) decomposition: Effect of the Ir particle size and metal-support interactions. *Catal. Lett.* **2018**, *148*, 341–347. [CrossRef]
34. Goula, M.A.; Charisiou, N.D.; Papageridis, K.N.; Delimitis, A.; Papista, E.; Pachatouridou, E.; Iliopoulou, E.F.; Marnellos, G.; Konsolakis, M.; Yentekakis, I.V. A comparative study of the H_2-assisted selective catalytic reduction of nitric oxide by propene over noble metal (Pt, Pd, Ir)/γ-Al_2O_3 catalysts. *J. Environ. Chem. Eng.* **2016**, *4*, 1629–1641. [CrossRef]
35. Li, H.; Hao, C.; Tian, J.; Wang, S.; Zhao, C. Ultra-durable Ni-Ir/$MgAl_2O_4$ catalysts for dry reforming of methane enabled by dynamic balance between carbon deposition and elimination. *Chem. Catal.* **2022**, *2*, 1748–1763. [CrossRef]
36. Nakagawa, K.; Ikenaga, N.; Suzuki, T.; Kobayashi, T.; Haruta, M. Partial oxidation of methane to synthesis gas over supported iridium catalysts. *Appl. Catal. A* **1998**, *169*, 281–290. [CrossRef]
37. Fiedorow, R.M.J.; Chahar, B.S.; Wanke, S.E. The sintering of supported metal catalysts. II. Comparison of sintering rates of supported Pt, Ir, and Rh Catalysts in hydrogen and oxygen. *J. Catal.* **1978**, *51*, 193–202. [CrossRef]

38. Argyle, M.D.; Bartholomew, C.H. Heterogeneous Catalyst Deactivation and Regeneration: A Review. *Catalysts* **2015**, *5*, 145–269. [CrossRef]
39. Yentekakis, I.V.; Goula, G.; Panagiotopoulou, P.; Kampouri, S.; Taylor, M.J.; Kyriakou, G.; Lambert, R.M. Stabilization of catalyst particles against sintering on oxide supports with high oxygen ion lability exemplified by Ir-catalysed decomposition of N_2O. *Appl. Catal. B Environ.* **2016**, *192*, 357–364. [CrossRef]
40. Goula, G.; Botzolaki, G.; Osatiashtiani, A.; Parlett, C.M.A.; Kyriakou, G.; Lambert, R.M.; Yentekakis, I.V. Oxidative Thermal Sintering and Redispersion of Rh Nanoparticles on Supports with High Oxygen Ion Lability. *Catalysts* **2019**, *9*, 541. [CrossRef]
41. Yentekakis, I.V. The effective-double-layer as an efficient tool for the design of sinter-resistant catalysts. In *Recent Advances in Electrochemical Promotion of Catalysis*; Vayenas, C.G., Vernoux, P., Eds.; Springer-Nature: Berlin/Heidelberg, Germany, 2023; pp. 117–149. Available online: https://link.springer.com/chapter/10.1007/978-3-031-13893-5_4 (accessed on 1 May 2023).
42. Royer, S.; Duprez, D.; Can, F.; Courtois, X.; Batiot-Dupeyrat, C.; Laassiri, S.; Alamdari, H. Perovskites as substitutes of noble metals for heterogeneous catalysis: Dream or reality. *Chem. Rev.* **2014**, *114*, 10292–10368. [CrossRef]
43. Zhu, J.; Li, H.; Zhong, L.; Xiao, P.; Xu, X.; Yang, X.; Zhao, Z.; Li, J. Perovskite oxides: Preparation, characterizations, and applications in heterogeneous catalysis. *ACS Catal.* **2014**, *4*, 2917–2940. [CrossRef]
44. Zhu, H.; Zhang, P.; Dai, S. Recent Advances of Lanthanum-Based Perovskite Oxides for Catalysis. *ACS Catal.* **2015**, *5*, 6370–6385. [CrossRef]
45. Peña, M.A.; Fierro, J.L.G. Chemical Structures and Performance of Perovskite Oxides. *Chem. Rev.* **2001**, *101*, 1981–2018. [CrossRef]
46. Yentekakis, I.V.; Georgiadis, A.G.; Drosou, C.; Charisiou, N.D.; Goula, M.A. Selective Catalytic Reduction of NO_x over Perovskite-Based Catalysts Using $C_xH_y(O_z)$, H_2 and CO as Reducing Agents—A Review of the Latest Developments. *Nanomaterials* **2022**, *12*, 1042. [CrossRef] [PubMed]
47. Evdou, A.; Georgitsis, T.; Matsouka, C.; Pachatouridou, E.; Iliopoulou, E.; Zaspalis, V. Defect Chemistry and Chemical Looping Performance of $La_{1-x}M_xMnO_3$ (M=Sr, Ca, (x = 0–0.5)) Perovskites. *Nanomaterials* **2022**, *12*, 3461. [CrossRef] [PubMed]
48. Gálvez, M.E.; Jacot, R.; Scheffe, J.; Cooper, T.; Patzke, G.; Steinfeld, A. Physico-chemical changes in Ca, Sr and Al-doped La–Mn–O perovskites upon thermochemical splitting of CO_2 via redox cycling. *Phys. Chem. Chem. Phys.* **2015**, *17*, 6629–6634. [CrossRef] [PubMed]
49. Matsouka, C.; Zaspalis, V.; Nalbandian, L. Perovskites as oxygen carriers in chemical looping reforming process—Preparation of dense perovskite membranes and ionic conductivity measurement. *Mater. Today Proc.* **2018**, *5*, 27543–27552. [CrossRef]
50. Nishihata, Y.; Mizuki, J.; Akao, T.; Tanaka, H.; Uenishi, M.; Kimura, M.; Okamoto, T.; Hamada, N. Self-regeneration of a Pd-perovskite catalyst for automotive emissions control. *Nature* **2002**, *418*, 164–167. [CrossRef] [PubMed]
51. Tanaka, H.; Uenishi, M.; Taniguchi, M.; Tan, I.; Narita, K.; Kimura, M.; Kaneko, K.; Nishihata, Y.; Mizuki, J. The intelligent catalyst having the self-regenerative function of Pd, Rh and Pt for automotive emissions control. *Catal. Today* **2006**, *117*, 321–328. [CrossRef]
52. Kousi, K.; Tang, C.; Metcalfe, I.S.; Neagu, D. Emergence and Future of Exsolved Materials. *Small* **2021**, *17*, 2006479. [CrossRef]
53. Cali, E.; Kerherve, G.; Naufal, F.; Kousi, K.; Neagu, D.; Papaioannou, E.I.; Thomas, M.P.; Guiton, B.S.; Metcalfe, I.S.; Irvine, J.T.; et al. Exsolution of Catalytically Active Iridium Nanoparticles from Strontium Titanate. *ACS Appl. Mater. Interfaces* **2020**, *12*, 37444–37453. [CrossRef] [PubMed]
54. Yang, L.; Jiao, Y.; Xu, X.; Pan, Y.; Su, C.; Duan, X.; Sun, H.; Liu, S.; Wang, S.; Shao, Z. Superstructures with Atomic-Level Arranged Perovskite and Oxide Layers for Advanced Oxidation with an Enhanced Non-Free Radical Pathway. *ACS Sustain. Chem. Eng.* **2022**, *10*, 1899–1909. [CrossRef]
55. Xu, X.; Wang, W.; Zhou, W.; Shao, Z. Recent Advances in Novel Nanostructuring Methods of Perovskite Electrocatalysts for Energy-Related Applications. *Small Methods* **2018**, *2*, 1800071. [CrossRef]
56. Yentekakis, I.V.; Konsolakis, M. Three-way Catalysis. In *Perovskites and Related Mixed Oxides*; Wiley-VCH, Vergal GmbH & Co. KGaA: Weinheim, Germany, 2016; pp. 559–586. [CrossRef]
57. Shen, M.; Zhao, Z.; Chen, J.; Su, Y.; Wang, J.; Wang, X. Effects of calcium substitute in $LaMnO_3$ perovskites for NO catalytic oxidation. *J. Rare Earths* **2013**, *31*, 119–123. [CrossRef]
58. Tarjomannejad, A.; Niaei, A.; Gómez, M.J.I.; Farzi, A.; Salari, D.; Albaladejo-Fuentes, V. NO+CO reaction over $LaCu_{0.7}B_{0.3}O_3$ (B = Mn, Fe, Co) and $La_{0.8}A_{0.2}Cu_{0.7}Mn_{0.3}O_3$ (A = Rb, Sr, Cs, Ba) perovskite-type catalysts. *J. Therm. Anal. Calorim.* **2017**, *129*, 671–680. [CrossRef]
59. Hwang, J.; Rao, R.R.; Giordano, L.; Katayama, Y.; Yu, Y.; Shao-Horn, Y. Perovskites in catalysis and electrocatalysis. *Science* **2017**, *358*, 751–756. [CrossRef] [PubMed]
60. Xu, X.; Pan, Y.; Ge, L.; Chen, Y.; Mao, X.; Guan, D.; Li, M.; Zhong, Y.; Hu, Z.; Peterson, V.K.; et al. High-Performance Perovskite Composite Electrocatalysts Enabled by Controllable Interface Engineering. *Small* **2021**, *17*, 2101573. [CrossRef]
61. Wang, M.; Zhao, T.; Dong, X.; Li, M.; Wang, H. Effects of Ce substitution at the A-site of $LaNi_{0.5}Fe_{0.5}O_3$ perovskite on the enhanced catalytic activity for dry reforming of methane. *Appl. Catal. B Environ.* **2018**, *224*, 214–221. [CrossRef]
62. Sim, Y.; Kwon, D.; An, S.; Ha, J.M.; Oh, T.S.; Jung, J.C. Catalytic behavior of ABO_3 perovskites in the oxidative coupling of methane. *Mol. Catal.* **2020**, *489*, 110925. [CrossRef]
63. Bashan, V.; Ust, Y. Perovskite catalysts for methane combustion: Applications, design, effects for reactivity and partial oxidation. *Int. J. Energy Res.* **2019**, *43*, 7755–7789. [CrossRef]

64. Bhattar, S.; Abedin, M.A.; Kanitkar, S.; Spivey, J.J. A review on dry reforming of methane over perovskite derived catalysts. *Catal. Today* **2021**, *365*, 2–23. [CrossRef]
65. Zou, G.; Wang, Z.; Sun, M.; Luo, X.; Wang, X. A novel solid-gas process to synthesize $LaMnO_3$ perovskite with high surface area and excellent activity for methane combustion. *J. Nat. Gas Chem.* **2021**, *20*, 294–298. [CrossRef]
66. He, L.; Fan, Y.; Bellettre, J.; Yue, J.; Luo, L. A review on catalytic methane combustion at low temperatures: Catalysts, mechanisms, reaction conditions and reactor designs. *Renew. Sustain. Energy Rev.* **2020**, *119*, 109589. [CrossRef]
67. Arai, H.; Yamada, T.; Eguchi, K.; Seiyama, T. Catalytic combustion of methane over various perovskite-type oxides. *Appl. Catal.* **1986**, *26*, 265–276. [CrossRef]
68. Luo, L.; Wang, S.; Wu, Z.; Qin, Z.; Zhu, H.; Fan, W.; Wang, J. Structure and performance of supported iridium catalyst for the lean methane oxidation at low temperature. *Appl. Catal. A* **2022**, *641*, 118699. [CrossRef]
69. Pliangos, A.; Yentekakis, I.V.; Papadakis, V.G.; Vayenas, C.G.; Verykios, X.E. Support-induced promotional effects on the activity of automotive exhaust catalysts: 1. The case of oxidation of light hydrocarbons (C_2H_4). *Appl. Catal. B* **1997**, *14*, 161–173. [CrossRef]
70. Vayenas, C.G.; Brosda, S.; Pliangos, C. The double-layer approach to promotion, electrocatalysis, electrochemical promotion, and metal–support interactions. *J. Catal.* **2003**, *216*, 487–504. [CrossRef]
71. Vernoux, P.; Lizarraga, L.; Tsampas, M.N.; Sapountzi, F.M.; DeLucas-Consuegra, A.; Valverde, J.L.; Souentie, S.; Vayenas, C.G.; Tsiplakides, D.; Balomenou, S.; et al. Ionically conducting ceramics as active catalyst supports. *Chem. Rev.* **2013**, *113*, 8192–8260. [CrossRef]
72. Papadakis, V.G.; Pliangos, C.A.; Yentekakis, I.V.; Verykios, X.E.; Vayenas, C.G. Development of high performance, Pd-based, three way catalysts. *Catal. Today* **1996**, *29*, 71–75. [CrossRef]
73. Konsolakis, M.; Drosou, C.; Yentekakis, I.V. Support mediated promotional effects of rare earth oxides (CeO_2 and La_2O_3) on N_2O decomposition and N_2O reduction by CO or C_3H_6 over Pt/Al_2O_3 structured catalysts. *Appl. Catal. B Environ.* **2012**, *123–124*, 405–413. [CrossRef]
74. Fornasiero, P.; Di Monte, R.; Ranga Rao, G.; Kaspar, J.; Meriani, S.; Trovarelli, A.; Graziani, M. Rh-loaded CeO_2-ZrO_2 solid-solutions as highly efficient oxygen exchangers: Dependence of the reduction behavior and the oxygen storage capacity on the structural properties. *J. Catal.* **1995**, *151*, 168–177. [CrossRef]
75. Botzolaki, G.; Goula, G.; Rontogianni, A.; Nikolaraki, E.; Chalmpes, N.; Zygouri, P.; Karakassides, M.; Gournis, D.; Charisiou, N.D.; Goula, M.A.; et al. CO_2 Methanation on Supported Rh Nanoparticles: The combined Effect of Support Oxygen Storage Capacity and Rh Particle Size. *Catalysts* **2020**, *10*, 944. [CrossRef]
76. Dalla Betta, R.A.; Rostrup-Nielsen, T. Application of catalytic combustion to a 1.5 MW industrial gas turbine. *Catal. Today* **1999**, *47*, 369–375. [CrossRef]
77. Haron, W.; Wisitsoraat, A.; Wongnawa, S. Comparison of monocrystalline $LaMO_3$ (M = Co, Al) Perovskite Oxide Prepared by Co-Precipitation Method. *Int. J. Chem. Eng. Appl.* **2014**, *5*, 123–126. [CrossRef]
78. Ponce, S.; Peña, M.A.; Fierro, J.L.G. Surface properties and catalytic performance in methane combustion of Sr-substituted lanthanum manganites. *Appl. Catal. B Environ.* **2000**, *24*, 193–205. [CrossRef]
79. Saracco, G.; Geobaldo, F.; Baldi, G. Methane combustion on Mg-doped $LaMnO_3$ perovskite catalysts. *Appl. Catal. B Environ.* **1999**, *20*, 277–288. [CrossRef]
80. Kaliaquine, S.; Van Neste, A.; Szabo, V.; Gallot, J.E.; Bassir, M.; Muzychuk, R. Perovskite-type oxides synthesized by reactive grinding: Part I. Preparation and characterization. *Appl. Catal. A* **2001**, *209*, 345–358. [CrossRef]
81. Patcas, F.; Buciuman, F.C.; Zsako, J. Oxygen non-stoichiometry and reducibility of B-site substituted lanthanum manganites. *Thermoch. Acta* **2000**, *360*, 71–76. [CrossRef]
82. Wang, S.; Zhang, Y.; Chu, P.; Liu, J.; Wang, M.; Zhang, P.; Duan, E. Different active sites of $LaCoO_3$ and $LaMnO_3$ for CH_4 oxidation by regulation of precursor's ion concentration. *Glob. Environ. Eng.* **2020**, *7*, 28–39. [CrossRef]
83. Nitadori, T.; Kurihara, S.; Misono, M. Catalytic properties of $La_{1-x}A'_xMnO_3$ (A' = Sr, Ce, Hf). *J. Catal.* **1986**, *98*, 221–228. [CrossRef]
84. Kröger, F.A.; Vink, H.J.; Seitz, F.; Turnbull, D. (Eds.) Relations between the concentrations of imperfections in crystalline solids. In *Solid State Physics*; Academic Press: Cambridge, MA, USA, 1956; Volume 3, pp. 307–435, ISBN 9780126077032. [CrossRef]
85. Nowotny, j.; Rekas, M. Defect chemistry of $(La,Sr)MnO_3$. *J. Am. Ceram. Soc.* **1998**, *81*, 67–80. [CrossRef]
86. Tang, W.; Wu, X.; Li, D.; Wang, Z.; Liu, G.; Liu, H.; Chen, Y. Oxalate route for promoting activity of manganese oxide catalysts in total VOCs' oxidation: Effect of calcination temperature and preparation method. *J. Mater. Chem. A* **2014**, *2*, 2544–2554. [CrossRef]
87. Hauptmann, W.; Votsmeier, M.; Gieshoff, J.; Drochner, A.; Vogel, H. Inverse hysteresis during the no oxidation on Pt under lean conditions. *Appl. Catal. B Environ.* **2009**, *93*, 22–29. [CrossRef]
88. Grunwaldt, J.D.; van Vegten, N.; Baiker, A. Insight into the structure of supported palladium catalysts during the total oxidation of methane. *Chem. Commun.* **2007**, *44*, 4635–4637. [CrossRef] [PubMed]
89. Al Soubaihi, R.M.; Saoud, K.M.; Dutta, J. Critical review of low-temperature CO oxidation and hysteresis phenomenon on heterogeneous catalysts. *Catalysts* **2018**, *8*, 660. [CrossRef]
90. Lashina, E.A.; Slavinskaya, E.M.; Chumakova, N.A.; Stadnichenko, A.I.; Salanov, A.N.; Chumakov, G.A.; Boronin, A.I. Inverse temperature hysteresis and self-sustained oscillations in CO oxidation over Pd at elevated pressures of reaction mixture: Experiment and mathematical modeling. *Chem. Eng. Sci.* **2020**, *212*, 115312. [CrossRef]
91. Chen, J.; Wang, X.; Zhang, L.; Rui, Z. Strong metal-support interaction assisted redispersion strategy for obtaining ultrafine and stable IrO_2/Ir active sites with exceptional methane oxidation activity. *Appl. Catal. B* **2021**, *297*, 120410. [CrossRef]

92. Wang, Y.; Arandiyan, H.; Tahini, H.A.; Scott, J.; Tan, X.; Dai, H.; Gale, J.D.; Rohl, A.L.; Smith, S.C.; Smith, R. The controlled disassembly of mesostructured perovskites as an avenue to fabricating high performance nanohybrid catalysts. *Nat. Commun.* **2017**, *8*, 15553. [CrossRef]
93. Reinke, M.; Mantzaras, J.; Schaeren, R.; Bombach, R.; Inauen, A.; Schenker, S. High-pressure catalytic combustion of methane over platinum: In situ experiments and detailed numerical predictions. *Combust. Flame* **2004**, *136*, 217–240. [CrossRef]